Key Points:
- This is the first study that uses a 3-D ice shelf-sea ice-ocean coupled model to represent the phytoplankton bloom of the Amundsen Sea Polynya
- Oceanic circulation plays two roles: provides dissolved iron to the polynya (meltwater pump) and also transports organic matter westward
- Model results improve our mechanistic understanding of the ASP bloom while suggesting testable hypotheses for future field efforts

Modeling the Seasonal Cycle of Iron and Carbon Fluxes in the Amundsen Sea Polynya, Antarctica

P. St-Laurent[1,2] [ID], **P. L. Yager[3]** [ID], **R. M. Sherrell[4,5]** [ID], **H. Oliver[3]** [ID], **M. S. Dinniman[1]** [ID], and **S. E. Stammerjohn[6]** [ID]

[1]Center for Coastal Physical Oceanography, Old Dominion University, Norfolk, VA, USA, [2]Virginia Institute of Marine Science, William & Mary, Gloucester Pt, VA, USA, [3]Department of Marine Sciences, University of Georgia, Athens, GA, USA, [4]Department of Marine and Coastal Sciences, Rutgers, State University of New Jersey, New Brunswick, NJ, USA, [5]Department of Earth and Planetary Sciences, Rutgers State University of New Jersey, Piscataway, NJ, USA, [6]Institute of Arctic and Alpine Research, University of Colorado Boulder, Boulder, CO, USA

Abstract The Amundsen Sea Polynya (ASP) is distinguished by having the highest net primary production per unit area in the coastal Antarctic. Recent studies have related this high productivity to the presence of fast-melting ice shelves, but the mechanisms involved are not well understood. In this study we describe the first numerical model of the ASP to represent explicitly the ocean-ice interactions, nitrogen and iron cycles, and the coastal circulation at high resolution. The study focuses on the seasonal cycle of iron and carbon, and the results are broadly consistent with field observations collected during the summer of 2010–2011. The simulated biogeochemical cycle is strongly controlled by light availability (dictated by sea ice, phytoplankton self-shading, and variable sunlight). The micronutrient iron exhibits strong seasonality, where scavenging by biogenic particles and remineralization play large compensating roles. Lateral fluxes of iron are also important to the iron budget, and our results confirm the key role played by inputs of dissolved iron from the buoyancy-driven circulation of melting ice shelf cavities (the "meltwater pump"). The model suggests that westward flowing coastal circulation plays two important roles: it provides additional iron to the ASP and it collects particulate organic matter generated by the bloom and transports it to the west of the ASP. As a result, maps of vertical particulate organic matter fluxes show highest fluxes in shelf regions located west of the productive central ASP. Overall, these model results improve our mechanistic understanding of the ASP bloom, while suggesting testable hypotheses for future field efforts.

Plain Language Summary Winds in the coastal Antarctic regions tend to create openings in the sea ice cover called "coastal polynyas." Such polynyas are found in multiple locations around the Antarctic continent including in the Amundsen Sea. This particular embayment features the fastest-melting ice shelves of the continent, but it is also distinguished by a large production of algae during the austral summer season. Recent studies have reported a statistical link between these two features but the mechanisms involved are not well understood. We use advanced computer simulations to gain insight into these mechanisms and use measurements collected in the Amundsen Sea to evaluate how realistic the simulations are. The results emphasize the two roles of the coastal circulation: it provides a necessary micronutrient (iron) to the algae and it also transports the algae away from where it grows during the summer. The computer simulations improve our understanding of why the Amundsen Sea Polynya is so productive, and they suggest new hypotheses that can be tested in future field efforts.

1. Introduction

Seaward directed katabatic winds in the coastal Antarctic regions tend to create openings in the sea ice cover called "coastal polynyas" (e.g., Morales Maqueda et al., 2004). Such polynyas are found in multiple locations around the Antarctic continent (Arrigo et al., 2015; Nihashi & Ohshima, 2015) including in the Amundsen Sea (Stammerjohn et al., 2015). This particular embayment features the fastest-melting ice shelves of the continent (Gardner et al., 2018; Rignot et al., 2013) as well as the most productive polynya per unit area (the Amundsen Sea Polynya, ASP). Based on remote sensing data for 1998–2014, Arrigo et al. (2015) estimate the net primary productivity of the ASP to be 105 g C·m^{-2}·year^{-1} and 0.8 g C·m^{-2}·day^{-1} on average over the

open water period. Satellite data suggest that the production is concentrated in December–February with a peak in January (Arrigo et al., 2015, their Figure 5) even though the polynya does not close until March (Stammerjohn et al., 2015).

A number of oceanographic expeditions have sampled the ASP during the austral summer period when the sea ice cover is minimal. A comprehensive biogeochemical data set was collected between 13 December 2010 and 8 January 2011 during the Amundsen Sea Polynya International Research Expedition (ASPIRE; Yager et al., 2012, 2016). Polynya-wide measurements show a large sink of atmospheric CO_2 (-0.43 ± 0.10 g C·m^{-2}·day^{-1} in the central polynya, -0.22 ± 0.17 g C·m^{-2}·day^{-1} on average) driven by biological activity (Mu et al., 2014). The bloom is dominated by one phytoplankton species (*Phaeocystis antarctica*) with surface particulate organic carbon (POC) reaching > 0.8 g/m^3 at multiple stations (0.57 ± 0.25 g/m^3 on average; Yager et al., 2016). The net primary productivity measured shipboard ranges from 1 to 4 g C·m^{-2}·day^{-1} among stations, with an average of 2.7 ± 0.85 g C·m^{-2}·day^{-1}. Another cruise conducted slightly later during the same months (21 December to 23 January; Lee et al., 2012) estimated the average net carbon uptake by phytoplankton at 2.2 ± 1.4 g C·m^{-2}·day^{-1}.

Observations collected later the following year indicate a rapid weakening of the bloom after January. Data from February 2012 show surface chlorophyll a (Chl a) concentrations ranging from 0.1 to 6 mg Chl a/m^3 among stations with an average of 3.1 ± 1.7 mg Chl a/m^3 (i.e., 0.15 ± 0.09 g C/m^3 assuming a mass ratio C:Chl $= 50$; Park et al., 2017). The average carbon uptake by phytoplankton in February/March 2012 is estimated at 0.2 ± 0.1 g C·m^{-2}·day^{-1} (B. K. Kim et al., 2015), significantly lower than observed earlier in the season during the previous year. Compared to December/January, these values represent a fourfold decrease in surface POC and a ninefold decrease in biological uptake. Hahm et al. (2014) proposed that decreased solar radiation and decreased iron availability are the likely causes of this rapid decline of the bloom. Indeed, incubation experiments by Alderkamp et al. (2015) show that the primary production in the ASP is stressed by limited iron availability while macronutrients are generally abundant. However, the few cruises conducted in this region and the scarce iron data provide only a fragmentary picture of the seasonal cycle of iron supply/demand.

This supply of iron to the ASP was examined by St-Laurent et al. (2017) in an idealized model setting. Following the observations of Sherrell et al. (2015), the iron sources included the following: (1) intrusions of offshelf water onto the continental shelf (primarily, modified Circumpolar Deep Water, mCDW), (2) sediments (e.g., Sherrell et al., 2018; Wadley et al., 2014), (3) ice shelves (Alderkamp et al., 2012; Gerringa et al., 2012), and (4) sea ice (Lannuzel et al., 2016). The study of St-Laurent et al. (2017) highlighted the important role of ice shelf melt-driven circulations (the "meltwater pump") in transporting sediment-derived dissolved iron (dFe) to the upper 300 m of the water column. However, removal processes (e.g., scavenging and phytoplankton uptake) that often play a critical role in shaping iron distributions (e.g., Bruland et al., 2014) were not included in that study. For example, the seasonal bloom of the polynya provides a large inventory of sinking biogenic particles that would favor iron removal throughout the water column.

In addition to their role as adsorptive scavenging phases, particles in the water column can also act as a source of dFe through remineralization of organic particles or the dissolution/solubilization of surface bound labile particulate iron (pFe). This dual role played by particles may have a large influence on iron distributions and can modulate the seasonal inventories in systems such as the ASP. For all these reasons, the inclusion of both dissolved and particulate forms of iron in numerical models is desirable.

Prior to this study, we simulated the bloom observed during ASPIRE (summer of 2010–2011) by modeling each station in a 1-D configuration. These modeling experiments combine realistic light, winds, and stratification with prescribed initial conditions (i.e., a finite inventory of dFe and dissolved inorganic nitrogen [DIN]) to examine the controls on primary production from October to March. The least constrained parameters of the biogeochemical model are optimized using the large data set of ASPIRE. The experiments highlight the importance of both light and iron limitation in determining the magnitude of the bloom. Light limitation grows with the bloom as a result of phytoplankton self-shading and continues over subsequent months as solar radiation declines (e.g., Park et al., 2017). dFe becomes increasingly limiting as the mixed layer inventory is consumed, contributing to the decreasing primary production. Finally, the simulations suggest that grazing pressure increases in March and accelerates the bloom decline.
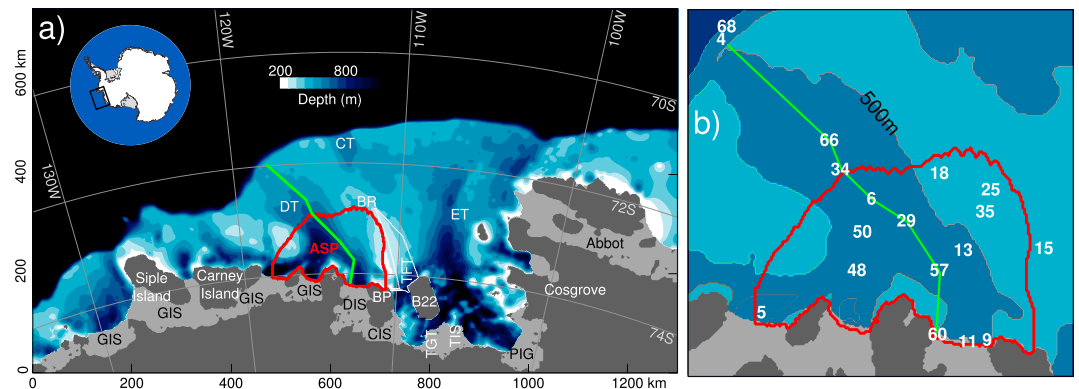
Figure 1. Model domain with the main ice shelves labeled. (a) The open boundaries of the model correspond to the edges of the figure. Color shading represents isobaths every 75 m. Features that are labeled are as follows: Dotson Trough (DT), Central Trough (CT), Eastern Trough (ET), Bear Ridge (BR), Amundsen Sea Polynya (ASP, red contour line), Getz Ice Shelf (GIS), Dotson Ice Shelf (DIS), Bear Peninsula (BP), Crosson Ice Shelf (CIS), Thwaites Glacier Tongue (TGT, white contour line), Thwaites Ice Shelf (TIS), B22 is a large grounded (static) iceberg, Thwaites Fast-ice Tongue (TFT), and Pine Island Glacier (PIG). The ASP represented is a climatological average for the month of January (years 2006–2011, Cavalieri et al., 2014). The green line is the section of Figure 3. (b) Location of ASPIRE stations.

In this study, we complement the observational studies and the 1-D modeling work by implementing a high-resolution 3-D model of the seasonal cycle in the ASP. The model includes advective processes and provides a quantitative representation of the annual nitrogen (N) and iron (Fe) cycles over multiple years (2006–2013). The study has two main objectives: (1) to describe the key processes that lead to seasonal supply and removal of iron in the ASP and (2) to provide insight on the fate of the POC produced by the bloom. The latter question is spatially and temporally complex (Lee et al., 2017; Mu et al., 2014; Yager et al., 2016), but these high-resolution model results may provide better estimates for the overall magnitude of the biological pump as contributed by Antarctic polynyas.

The study is structured as follows. In section 2 our modeling approach is described, including extensive model-data comparisons to highlight model strengths as well as weaknesses and purposeful omissions. The section 3.1 illustrates the seasonal cycle of iron within the polynya. The distributions are complemented by an iron budget (sections 3.2 and 3.3) clarifying the seasonality and magnitude of the processes affecting dissolved and pFe distributions. The section 3.4 examines the fate of POC during the simulated bloom.

2. Methods

Here we provide a description of the numerical model used in the study, an explication of the reservoirs and parameterizations used in the biogeochemical module that was developed specifically for the Amundsen Sea, and comprehensive comparisons between the model results and the observations collected during ASPIRE (Yager et al., 2012, 2016).

2.1. Physical Model

The study builds on an existing implementation (St-Laurent et al., 2017) of the Regional Ocean Modelling System (Shchepetkin & McWilliams, 2005) for the Amundsen Sea. It includes dynamic-thermodynamic sea ice (Budgell, 2005; Mellor & Kantha, 1989) and static ice shelves thermodynamically coupled to the ocean with transfer coefficients that are a function of the friction velocity (Dinniman et al., 2011; Holland & Jenkins, 1999). The model domain (see Figure 1) covers the entire Amundsen Sea continental shelf with a uniform horizontal mesh size of 1.5 km. The vertical dimension is discretized with 20 topography-following vertical levels (Shchepetkin & McWilliams, 2005).

The model topography and its atmospheric/oceanic boundary conditions are described in St-Laurent et al. (2017). The model simulations cover the period 1 January 2006 to 31 December 2013. The physical fields (currents, vertical mixing, salinity, temperature, sea ice, and ice shelf melt) are identical to those of the previous study (see St-Laurent et al., 2017, for various comparisons with observations). The present study differs by the inclusion of a biogeochemical module (described below) that is forced by the physical fields

at every baroclinic time step (90 s). All model fields are averaged in time and saved at daily resolution. No tidal forcing is applied to avoid aliasing by the daily outputs.

2.2. Biogeochemical Module

The biogeochemical module used in this study is based on the iron, nitrate, plankton, zooplankton, and detritus model of Fiechter et al. (2009) that is available in Regional Ocean Modelling System. However, a number of modifications are made to this model in order to address our particular research questions for the Amundsen Sea. This section provides a description and justification of the changes made, while the model equations are listed in the supporting information.

2.2.1. State Variables

The model represents the nitrogen and iron cycles with both cycles being largely symmetrical in regard to their state variables: DIN and dFe, phytoplankton nitrogen (N_P) and phytoplankton-iron (Fe_P), small detrital nitrogen (N_{SD}) and small detrital iron (Fe_{SD}), and large detrital nitrogen (N_{LD}) and large detrital iron (Fe_{LD}). The key differences between the nitrogen and iron cycles relate to grazing and to iron scavenging (section 2.2.4). The nitrogen cycle represents zooplankton explicitly as a variable $(N_Z$; as in the original model of Fiechter et al., 2009), while the iron cycle simply transfers the grazed phytoplankton-iron to the large detrital iron. This simplification avoids the need to track the iron fluxes associated with zooplankton.

The single phytoplankton variable represents *Phaeocystis antarctica* that dominated the bloom during ASPIRE (Yager et al., 2016). The model includes only one type of DIN that is equivalent to nitrate (nitrate generally dominates the DIN pool in the Amundsen Sea; see Yager et al., 2016). We did not attempt to parameterize dFe ligands, and colloidal iron is assumed to be a component of dFe (since no observations from the ASP were available to constrain these aspects). Nonbiogenic particles are not represented in the model. Biogenic pFe (bpFe) is defined as the sum of living phytoplankton-iron and small + large detrital iron. Particulate organic nitrogen (PON) is defined as the sum of phytoplankton, zooplankton, and small + large detrital nitrogen.

2.2.2. Phytoplankton Growth

The model represents phytoplankton growth as the product of a maximum growth rate ($P_{\max}$, in day^{-1}, described below), a nutrient availability, and a light availability:

$$P_{\max} \times \underbrace{\min\left(\frac{\mathrm{dFe}}{k_F + \mathrm{dFe}}, \frac{\mathrm{DIN}}{k_N + \mathrm{DIN}}\right)}_{\text{nutrient\ availability}} \times \underbrace{\frac{\alpha I}{\sqrt{\alpha^2 I^2 + P_{\max}^2}}}_{\text{light\ availability}}, \tag{1}$$

where I is the photosynthetically active radiation (PAR; see section 2.3) and α is described below. The overall nutrient availability is determined by the scarcer of DIN and dFe (Liebig's law of the minimum). Both DIN and dFe availability are parameterized using Michaelis-Menten kinetics and half-saturation constants specific to *Phaeocystis antarctica*: k_N = 2.5 mmol N/m^3 (Wang & Moore, 2011) and k_F = 0.26 nM (for colonial *Phaeocystis antarctica*; Garcia et al., 2009), respectively. The nutrient and light availability in equation (1) are dimensionless functions varying between 0 (absence of nutrients/light) and 1 (abundance of nutrients/light). Note that the model of Fiechter et al. (2009) focused on diatoms and included a process of "luxury uptake." We do not include this process because of our focus on *Phaeocystis antarctica* and the limited observations available from the ASP or other systems to constrain parameterization of this species.

The ratio of dFe and DIN uptake is assumed constant at a value (Fe:N = 0.013 μmol Fe/(mmol N), equivalent to Fe:C = 2 μmol Fe/(mol C), assuming Redfield) representative of *Phaeocystis antarctica* under iron-stressed/iron-limited conditions (Strzepek et al., 2011). The use of a constant ratio simplifies considerably the model and facilitates the interpretation of its results. The assumption of iron-stressed/iron-limited conditions is also consistent with the in situ experiments of Alderkamp et al. (2015) conducted during the rise in bloom biomass. However, we acknowledge that assuming a constant relatively low ratio may underestimate the rate of iron drawdown to limiting levels in the early part of the bloom (when dFe is relatively abundant).

The maximum growth rate ($P_{\max}$ = 1.6 day^{-1}) and the initial slope of the photosynthesis-irradiance curve (α = 0.06 m^2·W^{-1}·day^{-1}) are assumed to be constant in space/time (as in Fiechter et al., 2009), and their value is chosen to be representative of the central ASP (Figures 4c and 4d of Alderkamp et al., 2015). Note

that the constant P_{max} and α imply that the model does not allow for interactions between light and iron requirements (see Alderkamp et al., 2015 on this topic). While we recognize the importance of these interactions and their potential role in the ASP bloom, their inclusion is beyond the scope of this preliminary study and may be important to address in future studies.

2.2.3. Aggregation, Disaggregation, and Remineralization of Particles

We modify the model of Fiechter et al. (2009) by adding a second size class of particles (small and large) to both the nitrogen and iron cycles. The implementation follows Fennel et al. (2006) and includes the aggregation of slow-sinking small particles (living phytoplankton and small detritus) into faster-sinking large particles. Small detrital particles are formed through phytoplankton mortality, while large particles are formed through zooplankton mortality and small particle aggregation. Note that the model considers all large particles as "detritus" even when they are formed through aggregation of living phytoplankton.

Iron and nitrogen in both the small and large particles are remineralized at the same rate (which is constant in time and space for simplicity). One difference from Fennel et al. (2006) is that faster-sinking large particles slowly disaggregate back into small particles (e.g., Clegg et al., 1991) while they sink toward the seafloor. Without this process, the slow-sinking small particles tend to be remineralized in the upper water column and are unable to reach the deeper layers, leading to unrealistically low concentrations ($\sim$0) below 300 m. The disaggregation occurs at a rate constant in time/space of 10^{-2} day^{-1} for simplicity (experiments with rates of 10^{-3} and 10^{-1} day^{-1} showed no effects and unrealistically large effects, respectively).

2.2.4. Iron Scavenging

Iron scavenging corresponds to the adsorption of dFe onto particles present in the water column, followed by the gravitational sinking of those particles. Following Aumont et al. (2015, their equation 50), this removal process (in μmol Fe·m^{-3}·day^{-1}) is parameterized as the product of the concentration of particles and the concentration of dFe:

$$\text{scavenging}(x, y, z, t) = \text{constant} \times \text{particles}(x, y, z, t) \times \text{dFe}(x, y, z, t). \tag{2}$$

The dependence on particle concentration makes this a "second-order parameterization" in the classification of Tagliabue et al. (2016, their Table 1). For our implementation of this parameterization, small detritus concentrations (N_{SD}) are used as the "particle concentration" (a simplification based on the assumption that large particles contribute negligible surface area to any volume of seawater), while nonbiogenic particles are not represented in the model and thus do not contribute to iron scavenging. Aumont et al. (2015) propose constant = 0.005 (mmol C m^{-3})$^{-1}$·day^{-1} or, assuming Redfield, 0.033 (mmol N m^{-3})$^{-1}$·day^{-1}. For the purpose of this study we round this value to 0.05 (mmol N m^{-3})$^{-1}$·day^{-1}. Desorption of iron is not modeled (again because of lack of data), but iron is returned to the dissolved state from both small and large detritus during the process of remineralization.

2.2.5. Other Parameters of the Biogeochemical Module

Other parameters in the original model of Fiechter et al. (2009) were modified to reflect conditions in the ASP. The maximum grazing rate is set at 0.3 day^{-1} according to Yang et al. (2016). The sinking rate of living phytoplankton (0.05 m/day) is specific to *Phaeocystis antarctica*, while the sinking rate of small detrital particles (0.7 m/day) is representative of POC in the surface layers of West Antarctica (see Table 1 of Becquevort et al., 2001). Regarding the sinking rate of large particles, Wadley et al. (2014) conducted sensitivity experiments in a comparable model setting and suggested a value of 3.3 m/day to achieve realistic dFe concentrations. For the purpose of this study we round this value to 5 m/day and will show in the following sections that this choice yields reasonable carbon fluxes. The remineralization rate of particles (10^{-2} day^{-1}, constant in space/time) is not constrained by observations, but its magnitude is consistent with other modeling studies that use rates constant in space/time (e.g., Fennel et al., 2006) and with the particle mass budgets of Clegg et al. (1991).

The remaining parameters are poorly constrained and thus mostly follow earlier modeling studies. Phytoplankton and zooplankton mortality rates are set to 0.015 and 0.05 day^{-1}, respectively. For comparison, the corresponding rates of Aumont et al. (2015) are 0.01 and 0.03 day^{-1} (i.e., fairly close). The aggregation rate is 0.0025 $\left(\text{mmol} \quad \text{N m}^{-3}\right)^{-1}$·day^{-1} and within a factor of 2 of the value of Fennel et al. (2006). Finally, the grazing half-saturation constant and the zooplankton excretion constant are the same as in Fennel et al. (2006) and Fiechter et al. (2009), respectively.

2.3. Boundary Conditions for Nutrients, Biological Fields, and Light

DIN concentrations at the model open boundaries (see Figure 1 for their position) are set to 31 mmol N/m^3 throughout the water column and at all times. This value is representative of DIN concentrations prior to the development of the bloom (i.e., "Winter Water," see Table 2 of Yager et al., 2016). dFe concentrations at the model open boundaries are set to 0.37 nM if the water properties match those of mCDW (e.g., station 4 of Sherrell et al., 2015) and otherwise are set to 0. As in St-Laurent et al. (2017), mCDW is defined by a minimum depth of 250 m and a minimum temperature of 0.7 °C (a definition satisfied by all the layers positioned below the thermocline). The assumption of zero dFe above the mCDW layer frees us from prescribing a priori an unknown profile of dFe at the open boundaries. However, we note that this simplification may cause the model to underestimate dFe inputs since advection of mCDW is then the only way for dFe to enter the model domain at its lateral boundaries.

dFe concentrations next to the sea floor are relaxed toward a prescribed concentration to represent inputs from sediments. This concentration increases linearly with seafloor depth at depths greater than 300 m (see St-Laurent et al., 2017, for the justification). This sediment input is only prescribed on the continental shelf and outside of ice shelf cavities. The relaxation timescale is 30 days and is only active when the model concentration falls below the prescribed concentration (i.e., it only acts as a source of dFe).

Glacial melt contributes to dFe concentrations as in St-Laurent et al. (2017). This input is parameterized as a flux that varies in space/time and is proportional to ice shelf basal melt rates. The flux of dFe assumes a constant and uniform endmember of 20 nM for pure glacial meltwater (St-Laurent et al., 2017). We neglect the subglacial meltwater produced underneath the ice sheet as part of the subglacial hydrologic system (De'Ath et al., 2014) because of the large uncertainties surrounding the magnitude of this source (Hawkings et al., 2014), but we acknowledge that it may be an important component of the iron supply. Other sources of dFe such as atmospheric deposition, hydrothermal vents, and sea ice drainage/melt (Lannuzel et al., 2016) are neglected in this study. The neglection of dFe inputs from sea ice is suggested by observations (Sherrell et al., 2015) and earlier model results (St-Laurent et al., 2017). Overall, these choices represent conservative estimates for the supply of iron to the ASP.

All other biogeochemical inventories are set to very low values at the model open boundaries (e.g., Fennel et al., 2006): 10^{-3} mmol N/m^3 for phytoplankton, 10^{-1} mmol N/m^3 for zooplankton, 0 for detrital nitrogen, and 10^{-3} nM for detrital iron (i.e., the nonliving bpFe). The small imposed values at the open boundaries ensure that the simulated biomass is of 'local' origin (inside the Amundsen Sea embayment).

The PAR immediately above the sea surface (denoted as 0$^+$) is assumed to be proportional to the 3-hourly surface downwelling shortwave radiation of ERA-Interim (SW, Dee et al., 2011). Ship observations collected during ASPIRE suggest the relation PAR(0$^+$) $\approx$ 0.64 SW. Vertical PAR profiles (84 total) collected during the same cruise suggest that the PAR immediately below the surface (0$^-$) can be approximated as PAR(0$^-$)/PAR(0$^+$) $\approx$ 0.84 − 0.0071 $zeni$, where $zeni$ is the Sun zenith angle. The same PAR profiles were combined with observed profiles of chlorophyll (converted to nitrogen assuming a mass ratio C:Chl=50 and Redfield C:N) to derive a parameterization of the light attenuation (k_d, m^{-1}) due to phytoplankton ("self-shading"): $k_d \approx 0.04 + 0.04 N_P$, where the first term is the absorption due to "pure seawater" (e.g., Fennel et al., 2006) and N_P is the phytoplankton concentration in mmol N/m^3.

2.4. Numerical Simulations Conducted

The biogeochemical model was initialized on 1 January 2006 with all state variables set to 0 except DIN (31 mmol N/m^3 uniformly; see section 2.3). The model then underwent an 8-year-long spin-up (1 January 2006 to 31 December 2013) to allow dFe and other variables to build up and stabilize. The conditions on 31 December 2013 were then used as the initial condition for an additional 8-year period (1 January 2006 to 31 December 2013). All the results presented in this study are for the second 8-year simulation. Note that this spin-up procedure only applies to the biogeochemical variables (not the physical fields). The physical fields used in the two 8-year simulations are the same as in St-Laurent et al. (2017; see this reference for more information and for comparisons with physical observations).

2.5. Calculation of Vertical Carbon Fluxes

Vertical carbon fluxes are calculated as the product of PON concentrations and sinking velocities and assume C:N=106:16 (Redfield). The sinking velocity of large detritus is ~7 times that of small detritus (section 2.2), and thus, the former generally dominates the modeled flux. The modeled fluxes are compared against obser-
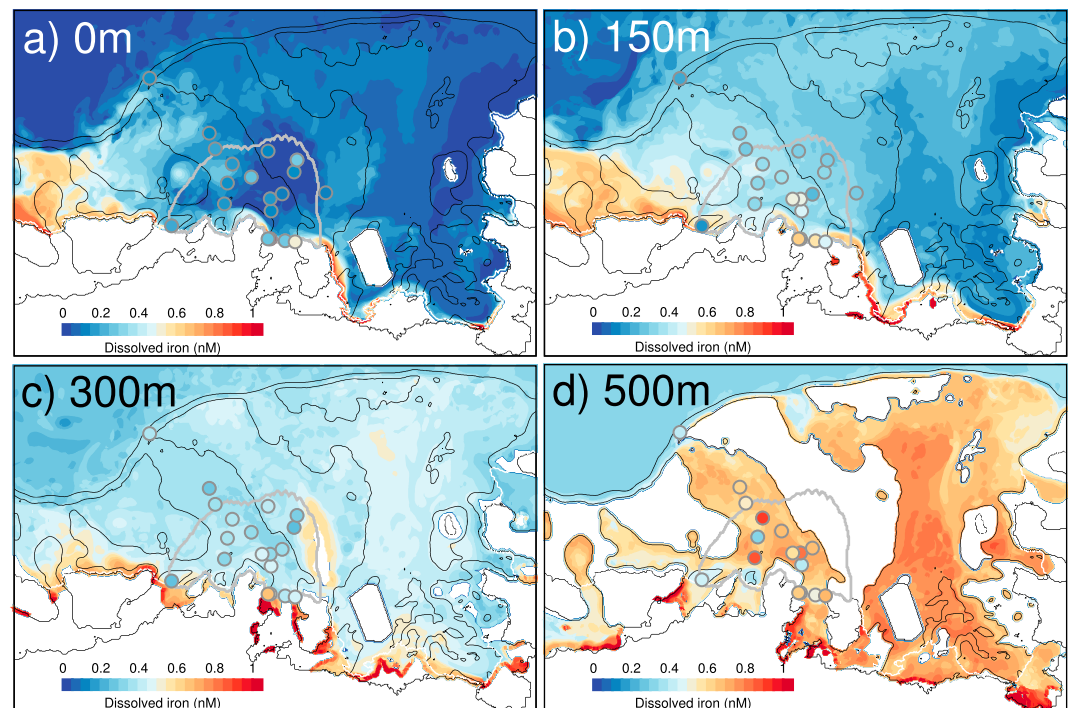
Figure 2. Horizontal distribution of dissolved iron (dFe). Observations from Amundsen Sea Polynya International Research Expedition are represented by colored circles; contoured values are modeled fields (averaged between 15 December 2010 and 15 January 2011) at depths of (a) 0, (b) 150, (c) 300, and (d) 500 m. Black contour lines represent the grounding line and the 500- and 1,000-m isobaths. The gray contour line is the climatological extent of the polynya in January.

vations (section 2.6) from two short-term (2–3 days) drifting traps released during ASPIRE at depths of 60, 150, and 300 m (Yager et al., 2016) and from a long-term moored trap at 350 m at Station 57 (Ducklow et al., 2015).

2.6. Evaluation of the Model Results Against Observations

The simulated dFe inventory is compared to the ASPIRE data set in Figure 2. The figure represents an average of model output over the cruise period and shows all the data collected for each depth horizon. The model captures the top-to-bottom variations as well as the enhanced concentrations at the ice shelf front (150- and 300-m depths). Notable biases include an underestimation near the Getz Ice Shelf at 150-m depth (Station 5; see Figure 1b for the location of the stations). The modeled distribution is also smoother than observations at 500 m (a consequence of the simple parameterization of sediment sources; see St-Laurent et al., 2017).

The dFe, bpFe, and PON concentrations are compared to the ASPIRE data set along a vertical section from the Dotson ice shelf front to the shelf break, following the Dotson Trough (Figure 3; see Figure 1 for the position of the transect). Again, the model captures the top-to-bottom variations of dFe as well as the higher concentrations at the ice shelf front. Biogenic pFe shows highest concentrations in the surface layers and a broader and weaker secondary maximum around 500 m (these vertical variations will be examined in more detail in the next section). Finally, modeled PON exhibits highest concentrations in the surface layers and a rapid decrease with depth. These variations are generally consistent with the data although the modeled fields are smoother than the observations.

The seasonal evolution of the bloom is compared to the ASPIRE data in Figures 4a–4c for a station representative of the center of the polynya (Station 29; see Figure 1b for the location of stations). The figure is limited to the upper 160 m to highlight the biological activity which appears to be captured reasonably well by the model. Accumulation of PON and nutrient drawdown begin shortly after the opening of the polynya (December) and continue until February/March. The DIN drawdown and PON are mainly concentrated in a shallow mixed layer (~15 m). Scavenging, driven by the production of biogenic particles (equation (2)),
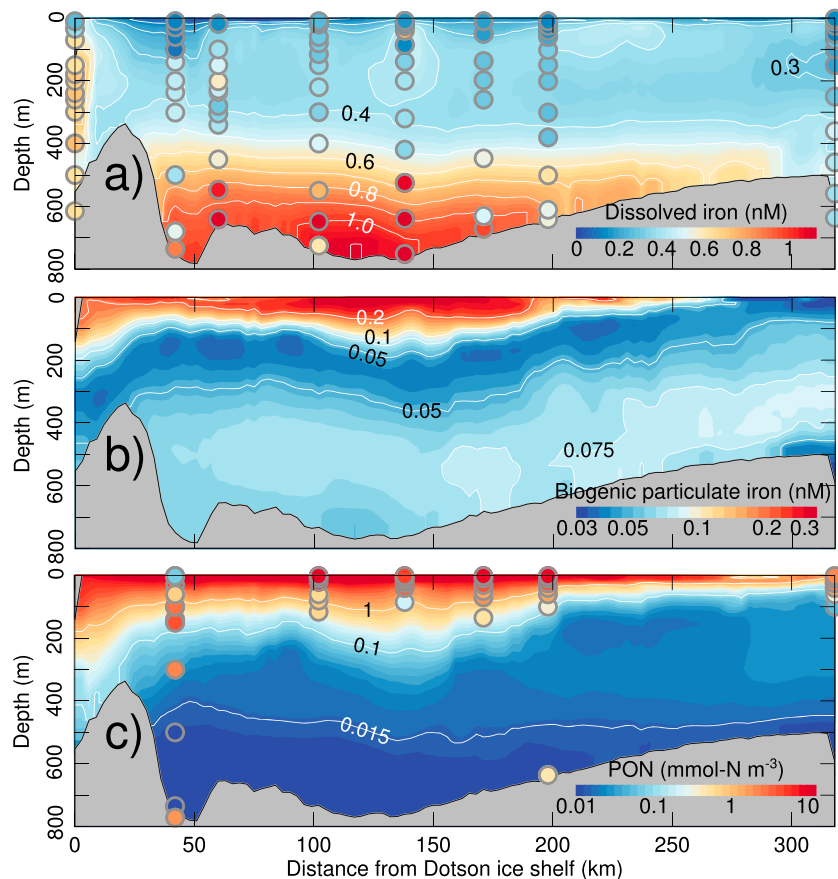
Figure 3. Vertical distributions from the Dotson Ice Shelf to the shelf break (see Figure 1 for the location of the section, green). (a) Dissolved iron (dFe), (b) biogenic particulate iron (bpFe), and (c) particulate organic nitrogen (PON). Observations from Amundsen Sea Polynya International Research Expedition are represented by colored circles; contoured values are modeled fields averaged between 15 December 2010 and 15 January 2011. Note the log scale in (b) and (c).

effectively removes dFe down to 160 m. All three fields show high-frequency variations (timescales of a few days) associated with mesoscale activity and wind events. The model biases include an underestimation of the mixed layer depth ($\geq$20 m in the data) and an overestimation of dFe in the upper 20 m (0.15–0.3 nM in the data, 0.35 nM in the model).

The seasonal evolution of the simulated bloom is qualitatively similar at the other stations (see supporting information) with the southern stations being the most affected by the surface overestimation of dFe. For example, Station 48 exhibits inputs of dFe in the upper 60 m in August–November (Figures 4d–4f), which are associated with the buoyant outflow from the ice shelves. As mentioned in St-Laurent et al. (2017), the model most likely overestimates the buoyancy of this outflow because of the lack of tidal mixing within the cavities (e.g., Jourdain et al., 2019), which would contribute to the surface overestimation of dFe. Additional iron data covering multiple seasons would be necessary to test hypothetical mechanisms for these model-data discrepancies.

The simulated vertical carbon flux is compared against observations (described in section 2.5) in Figure 5. The simulated vertical flux increases rapidly in early December and decreases gradually over the following months. The maximum flux is concentrated between mid-December and late January at a depth of 60 m and tends to occur later with increasing depth. Between April and September the simulated fluxes are comparable in magnitude throughout the upper 300 m as wintertime mixing homogenizes PON concentrations over this depth interval. The model generally reproduces the order of magnitude of the flux at the depths sampled. However, the flux at 300 and 350 m appears delayed compared to the trap data. The 350-m trap shows values ~1 mmol C·m^{-2}·day^{-1} in late December, while the modeled flux at the same depth reaches compara-
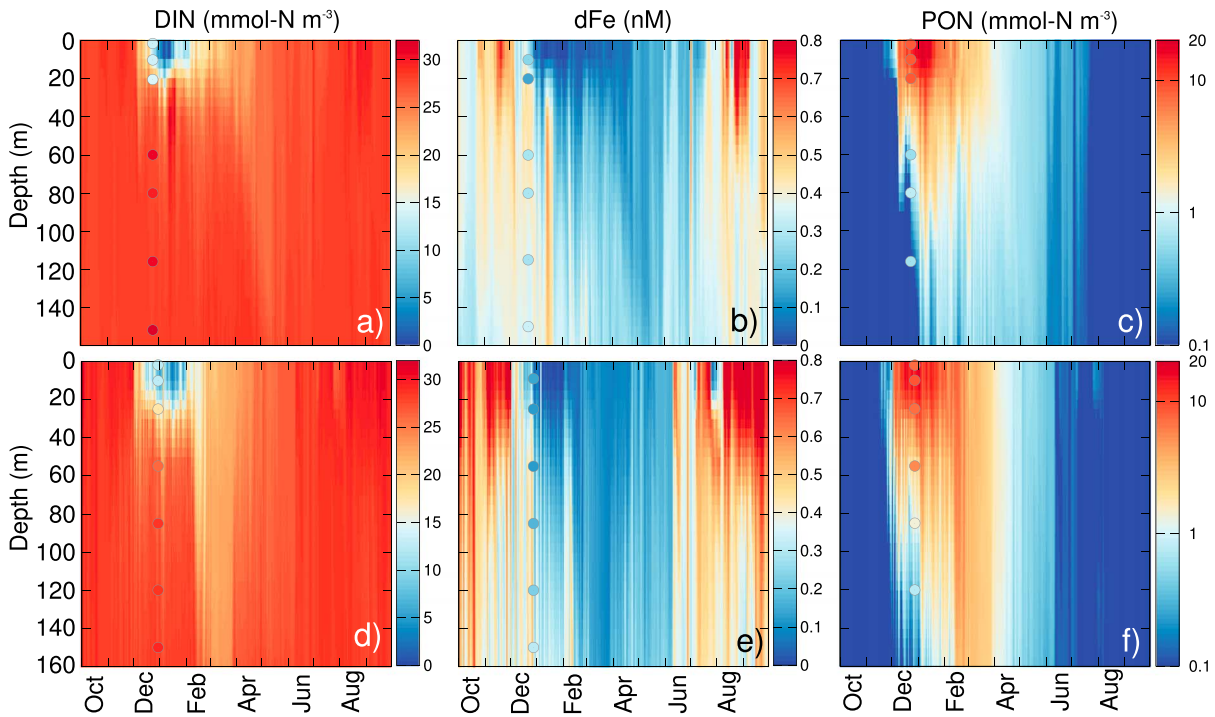
Figure 4. Seasonality of nutrients (dissolved inorganic nitrogen [DIN] and dissolved iron [dFe]) and particulate organic nitrogen (PON, October 2010 to September 2011) at two representative individual stations of the polynya occupied during the ASPIRE cruise. (a–c) Station 29 (center of the polynya; see Figure 1b for locations). (d–f) Station 48. Observations from ASPIRE are represented by colored circles; contoured values are modeled fields. Note the log scale used for PON. Additional stations can be seen in the supporting information.

ble values approximately 2 weeks later. Also, the 350-m trap shows a rapid increase from mid-December to mid-January (and lower values over the rest of the year), while the model suggests a broad peak from January to May at this depth. Despite these discrepancies in the timing of the flux, the POC flux accumulated by the moored trap during its > 1-year deployment (18 December 2010 to 4 January 2011) is within 20% of the simulated flux over the same period (315 mmol C/m² for the mooring (Ducklow et al., 2015) and 364 mmol C/m² for the model).
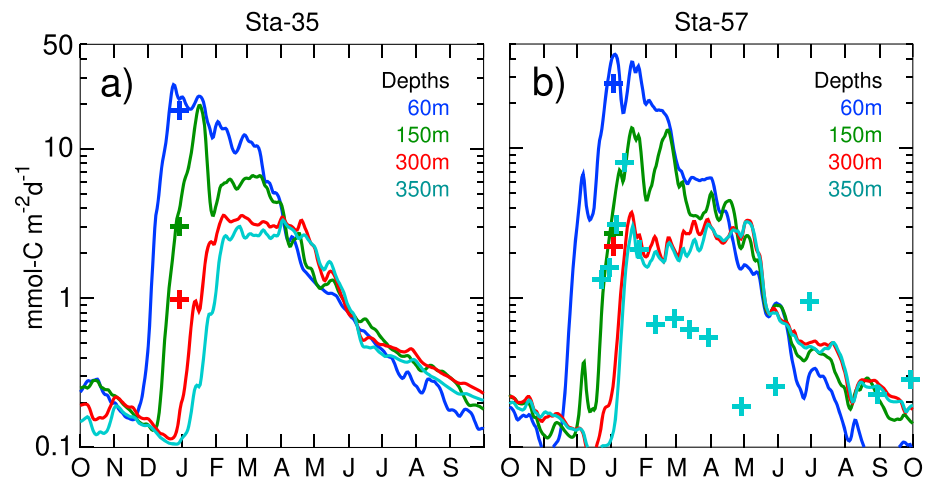

Figure 5. Vertical carbon flux at Stations 35 and 57 during the Amundsen Sea Polynya International Research Expedition period (austral summer 2010–2011). The modeled flux is smoothed (cutoff frequency of 1/15 days) and shown at four depth horizons. Blue, green, and red crosses are from drifting sediment traps released at the two stations (see Yager et al., 2016), while the cyan crosses are from a moored trap at Station 57 (Ducklow et al., 2015).
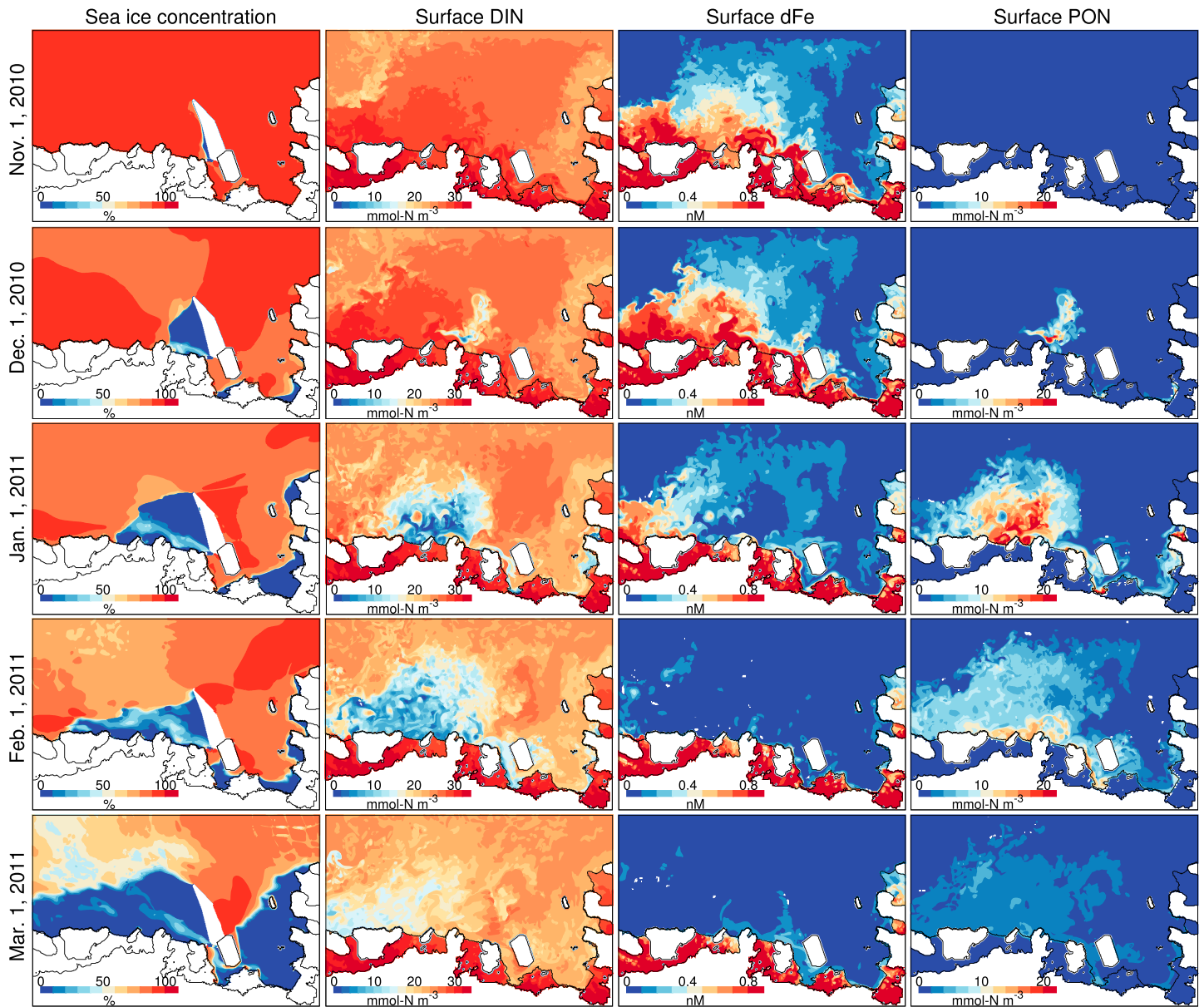
Figure 6. Simulated sea ice concentration, surface nutrients (dissolved inorganic nitrogen [DIN] and dissolved iron [dFe]) and surface particulate organic nitrogen (PON) during the summer 2010–2011. The figure illustrates the typical evolution of the simulated summer bloom. A video showing the same fields at daily interval can be downloaded from the supporting information (Movie S1).

3. Results

3.1. Spatial and Temporal Distributions of Key Biogeochemical Fields

The biogeochemical fields exhibit considerable horizontal variability during the simulated summer bloom (Figure 6; see also Movie S1 in the supporting information). Prebloom conditions (1 November) feature a large onshore dFe gradient due to the meltwater pump (see St-Laurent et al., 2017) with surface concentrations ≤0.1 nM beyond the shelf break. This meltwater-driven dFe input extends farther offshore over the Dotson Trough as expected from its recirculating clockwise gyre (St-Laurent et al., 2017, their Figure 8). Surface concentrations are comparatively low in the Eastern Trough (≤0.1 nM) given the westward current near the coast (carrying dFe away) and the assumption of zero surface dFe coming from the model's open boundaries (in this case from the Bellingshausen Sea; see section 2.3).

The opening of the ASP is followed rapidly by accumulation of PON and nutrient drawdown (early December, Figure 6). The bloom generally expands from east to west in reaction to the retreating sea ice cover
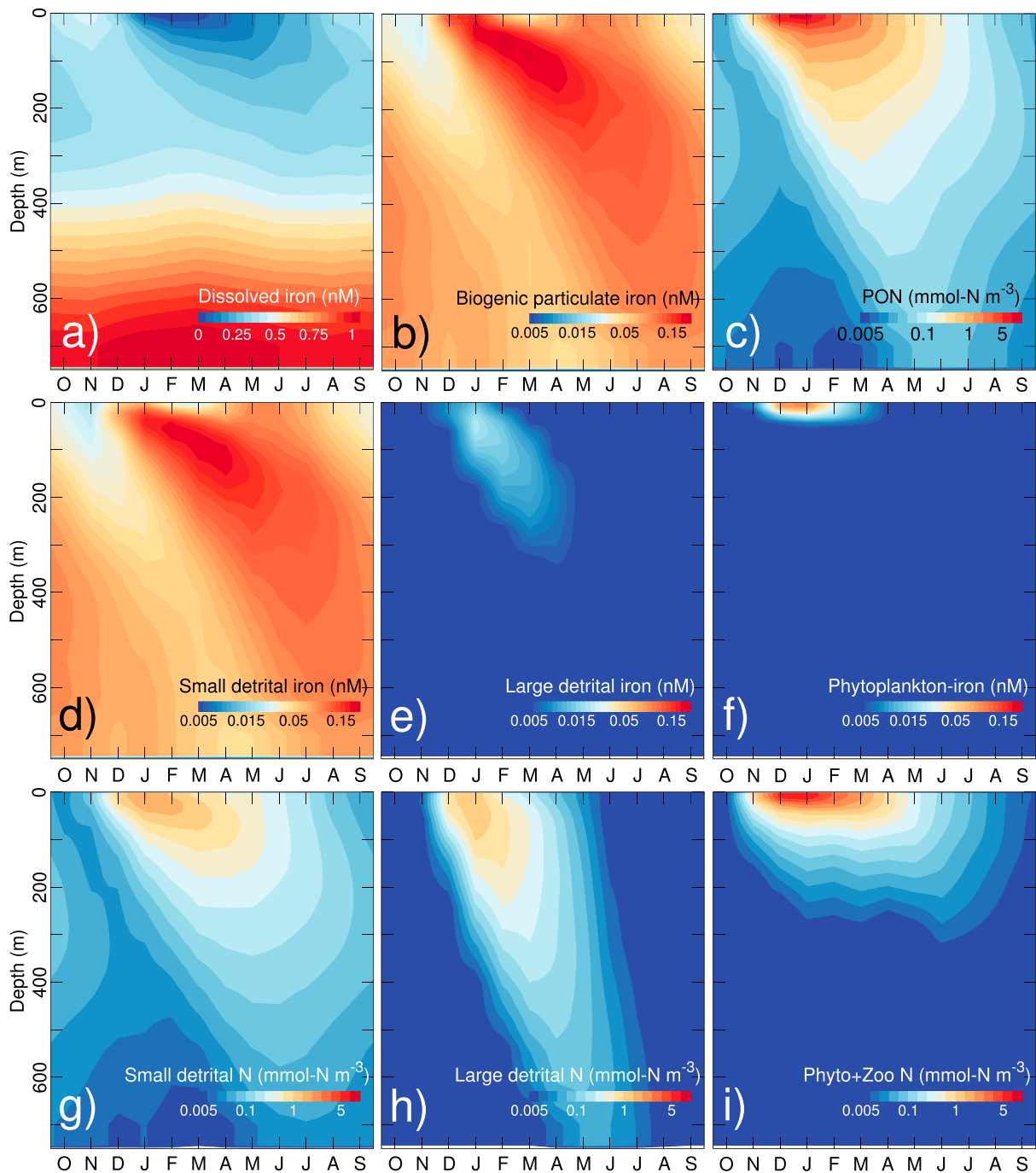
Figure 7. Seasonality of modeled distributions at the center of the polynya (Station 29; see Figure 1b for the location of the stations). (a) Dissolved iron (dFe), (b) biogenic particulate iron (bpFe), and (c) particulate organic nitrogen (PON). The second and third rows decompose bpFe and PON into their respective individual components (see section 2). The profiles are averaged over 2006–2013. Note the linear scale in (a) and the log scale in the other figures.

and increased light availability. The higher sea ice concentrations over the eastern trough and the rest of the domain leads to comparatively low PON concentrations (except in the immediate vicinity of Pine Island Glacier and Thwaites). PON concentrations reach their seasonal maximum in January but continue to expand laterally over the following months due to advection by the oceanic circulation. Both PON and nutrient fields exhibit small-scale spatial variability associated with mesoscale eddies (length scales of 5–30 km), causing small-scale variations in surface DIN of ±10 mmol N/m^3 or greater.

Surface nutrient concentrations in February reach < 5 mmol N/m^3 for DIN and < 0.1 nM for dFe (Figure 6). The nutrient depletion is largest at the surface under the simultaneous action of biological uptake and scavenging (in the case of iron). The meltwater pump continues to supply dFe throughout February and the maximum PON concentrations during this period are found near the ice shelf front (Figure 6).

Substantial variations are apparent in the vertical profiles of the biogeochemical fields over the course of the year (Figure 7). Profiles of dFe are dominated by high concentrations in the lower half of the water column (the contribution from sediments) and by iron removal from the surface down to 300-m depth. The lowest dFe concentrations are found near the surface around March and the surface concentrations subsequently increase as the water column becomes increasingly mixed (wintertime mixing). The profiles of bpFe and PON share multiple features including highest surface concentrations in January (summer bloom) and lowest surface concentrations in October–November (onset of the bloom). Both fields exhibit a "slanted" structure associated with the slow sinking of organic material produced during the summer bloom. This sinking is apparent over a period of 6 months so that the seasonal cycle of surface and bottom PON concentrations are approximately out of phase by ∼180°.

Despite their similarities, the profiles of bpFe and PON exhibit important differences over the seasons (Figures 7b and 7c). First, iron scavenging implies that bpFe gradually accumulates iron as it sinks into the iron-rich bottom layers. This is particularly apparent in the winter period when bpFe concentrations actually increase with depth (a feature virtually absent in PON profiles). The same feature appears as a deep secondary maximum in Figure 3b (see section 2.6). More generally, iron scavenging causes Fe_{SD} to overshadow Fe_{LD} and Fe_P (Figures 7d–7f). This is in contrast to the components of PON whose concentration are roughly comparable in the upper 200 m (Figures 7g–7i). Interestingly, the model suggests that surface concentrations of Fe_{SD} reach a minimum in February–March (Figure 7d). This particular period is characterized by very low surface dFe concentrations that limit scavenging in this part of the water column at this time of the year (equation (2)). Below the surface mixed layer, dFe concentrations are sufficiently high for scavenging to persist and for Fe_{SD} to increase between January and March. The surface minimum lasts until winter mixing resupplies the surface layers with small detrital particles (April–June). These seasonal variations and the processes responsible for them are examined in further detail in the next section.

3.2. Iron Cycling Within the Polynya

We use an iron budget to quantify the processes driving the seasonal cycle of iron within the polynya. To facilitate the interpretation of the budget, we represent the polynya as a control volume (Figure 1) whose shape is fixed in time. Its horizontal extent is calculated with a maximum 15% sea ice concentration threshold (using the data of Cavalieri et al., 2014) and represents a climatological average (years 2006–2011) for the month of January (i.e., the month when the production is maximal according to Arrigo et al., 2015). The area of the control volume is 25.3 × 10^9 m^2, and the mean bottom depth inside this area is 598 m. The control volume here includes the whole water column (surface to bottom) to provide a complete picture of iron cycling within the polynya. Oceanic advection is represented in the budget as a horizontal flux that enters/leaves the control volume at each point of its perimeter. The net flux obtained by integration around the perimeter is referred to as the "lateral flux." Finally, the iron budget discriminates between dFe and bpFe (small and large bpFe combined).

The seasonal budget of dFe is dominated by iron scavenging and by remineralization (Figure 8a). Both processes occur throughout the water column and are strongly modulated by the biological production. Scavenging increases rapidly in December and January in response to the newly available biogenic particles. Over the rest of the year, scavenging decreases gradually as biogenic particles are remineralized and eventually the two processes balance each other (August–November, Figure 8a). Positive lateral fluxes occur over most of the year and supply dFe to the control volume (note that this topic is examined in more detail in section 3.3). Biological uptake is the smallest term of the budget as expected from a process that is limited to the shallow mixed layer (the other processes occur throughout the water column). The net change from all these processes is a decrease during the production period and a gradual recovery from January–June (from remineralization and positive lateral fluxes).

The budget of bpFe (Figure 8b) is, to a large extent, a mirror image of dFe since the sinks become sources (and vice versa). Notable features include a negative lateral flux of bpFe following the summer bloom. This negative flux represents a horizontal transport of biogenic material out of the control volume (as expected if an area has higher production than its surroundings). The budget of bpFe also includes an extra term
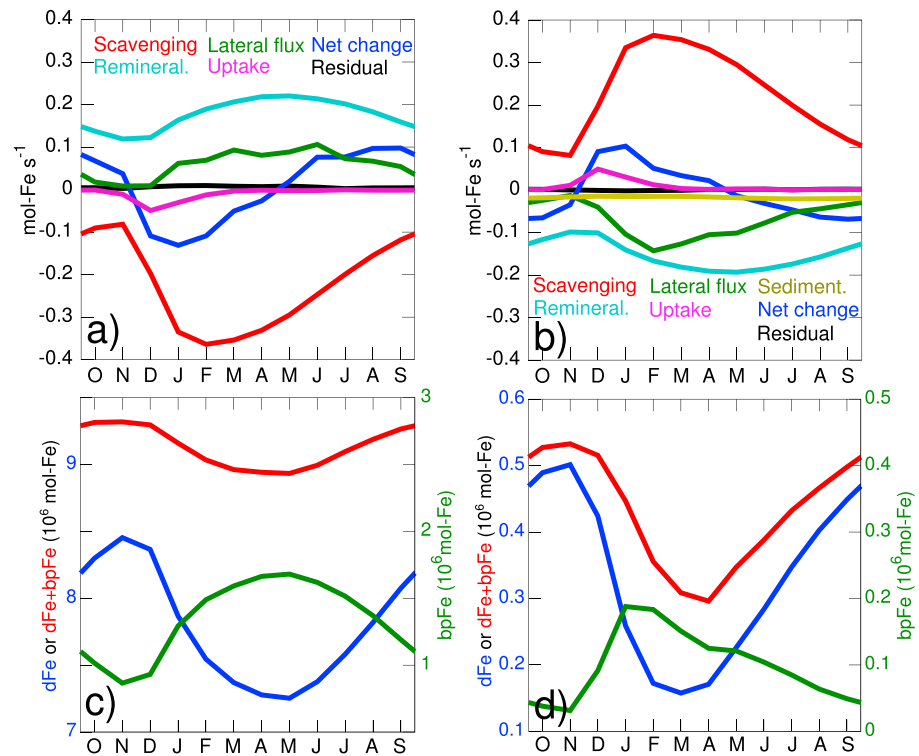
Figure 8. Seasonal iron budget for the control volume. The volume corresponds to the red contour line in Figure 1. (a) Budget of dissolved iron (dFe) for the entire water column. "Net change" is the temporal derivative of dFe inventory. "Residual" represents the budget closure. (b) Budget of biogenic particulate iron (bpFe) for the entire water column. (c) Inventory of dFe, bpFe, and dFe + bpFe in the water column. (d) Same as (c) but in the upper 100 m. The terms are averaged over 2006–2013.

(sedimentation) representing the loss from the water column. This term is comparatively small throughout the year as the bulk of the biogenic particles are either transported out of the control volume by the horizontal circulation or remineralized before they reach the sea floor (bottom depths are up to 1000 m in parts of the control volume).

Water column inventories of dFe and bpFe also exhibit mirror image behavior (Figure 8c). The dFe inventory decreases rapidly after December and then recovers from May to November (the opposite for bpFe). At first view, the control volume thus resembles an isolated system with only internal exchanges between its dFe and bpFe pools (and no change in dFe + bpFe). However, the time series of dFe + bpFe indicates that this relation between dFe and bpFe is only approximate (Figure 8c). The lateral export of bpFe causes a decrease in dFe + bpFe from January to March, and the lateral import of dFe drives the recovery of dFe + bpFe from June to September. Overall, the seasonal change in dFe+bpFe is approximately one third of that of dFe or bpFe.

The results discussed above are for the water column as a whole. Additional information can be gained by examining the inventories just in the upper 100 m of the control volume (Figure 8d). In this case, the inventory of dFe + bpFe tends to follow the dFe inventory. Both exhibit a large decrease during the production period and a gradual recovery from May to September. The summer increase in the bpFe inventory is approximately half the magnitude (total moles) of the decrease in dFe inventory. Moreover, a temporal asymmetry is apparent between the dFe and bpFe pools, with bpFe reaching its maximum two months before dFe attains its minimum (January and March, respectively). This disconnect between dFe and bpFe inventories is caused, presumably, by vertical sinking that removes bpFe from the upper 100 m before it can be remineralized, but with long enough residence of Fe_{SD} in the upper 100 m to effect continued scavenging of dFe. Differences in the lateral flux of dFe and bpFe may also contribute to the disparity.

Further insight into the seasonal bloom is gained by focusing on the factors affecting living phytoplankton-iron (light and nutrient availability; Figure 9). For this analysis, the light/nutrient terms (see section 2.2.2) are spatially averaged over the phytoplankton biomass of the control volume. Such a
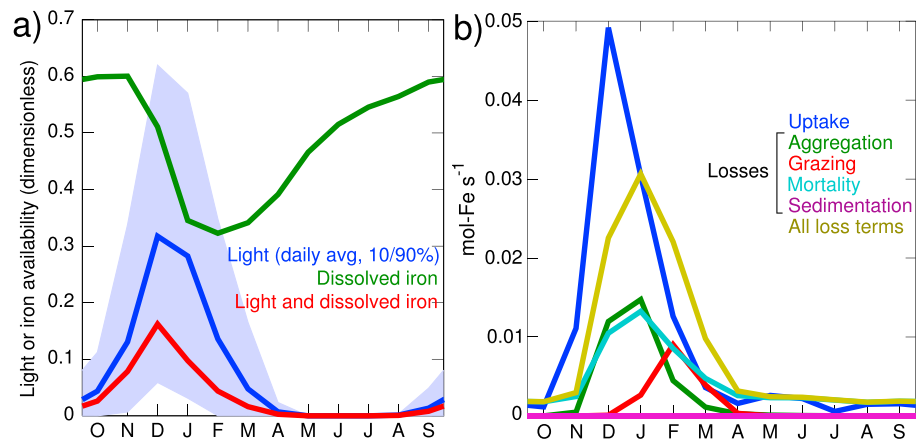
Figure 9. Light and iron availability and sources/losses of living phytoplankton-iron (Fe_P) inside the control volume. The volume corresponds to the red contour line in Figure 1. (a) Availability of light and iron to phytoplankton in the surface mixed layer (equation (1)). The blue shading is the 10th/90th percentile representing the daily variation around the mean. (b) Source and loss terms of Fe_P integrated from the surface to the bottom. Biological uptake (blue curve) is a source while the other four terms represent losses. "Sedimentation" is the flux of Fe_P at the water-sediment interface and is generally zero. The terms are averaged over 2006–2013.

spatial averaging is equivalent to an average over the surface mixed layer (where living phytoplankton reside). Note also that despite its low concentrations at the surface during the bloom (Figure 6), DIN is generally more available than dFe and thus the figures focus on the latter. Overall, the seasonal bloom exhibits the same qualitative features as in our earlier 1-D simulations. From October to December, dFe is relatively abundant while light availability increases in response to sea ice retreat. After December, phytoplankton self-shading and decreasing solar radiation reverse this trend and force a gradual decline in light availability. Light and iron availability are both ~ 0.3 in January (equivalent to a mixed-layer dFe concentration of 0.13 nM). Iron is more limiting than light at local noon (the daily light cycle is represented by a shading in Figure 9a) in December–January but light becomes far more limiting in February and later months. The combined light/iron availability suggests a peak phytoplankton growth in December. Notable differences from the 1-D simulations include a slower decrease in dFe availability during the production period (December–February), and a higher minimum availability, suggestive of an advective input of dFe (see section 3.3).

The losses of living phytoplankton and their associated iron are integrated from the surface to the bottom and shown in Figure 9b. The sum of all the loss terms is comparable in magnitude to biological iron uptake in the month of January, and it becomes greater than the biological iron uptake in the following months. Aggregation and mortality are comparable in magnitude during December–January and nearly account for all the losses during this period. Note that the aggregation of living phytoplankton into larger particles is considered an immediate loss since the model assumes all large particles to be detritus (see section 2). In the subsequent months, the losses are primarily due to mortality, grazing and, to a lesser extent, aggregation. The smallest term, sedimentation, represents the vertical flux of living phytoplankton at the water-sediment interface and is negligible throughout the year. These features are, overall, similar to the seasonal bloom described in of the 1-D simulations except for the grazing loss. This term plays a key role in terminating the bloom of the 1-D model while the 3-D model suggests a smaller role distributed over the summer period.

3.3. Iron Supply in Presence of Iron Removal Processes
The results from the previous sections suggest that dFe is being supplied to the polynya during the summer bloom (Figure 6) and after the bloom (Figure 8a). These transport pathways were examined in St-Laurent et al. (2017), but iron removal processes were not included in that source-tracing study (dFe was treated unrealistically as a conservative property). We revisit this issue here and consider the fluxes of dFe to a control volume (Figure 1) that includes the entire water column (surface to bottom; Figure 10a). Since we consider the entire water column, dFe is supplied by horizontal advection at the edge of the polynya (primarily the westward coastal current; see Figure 10b) and supplied by the meltwater pump at the ice shelf fronts.
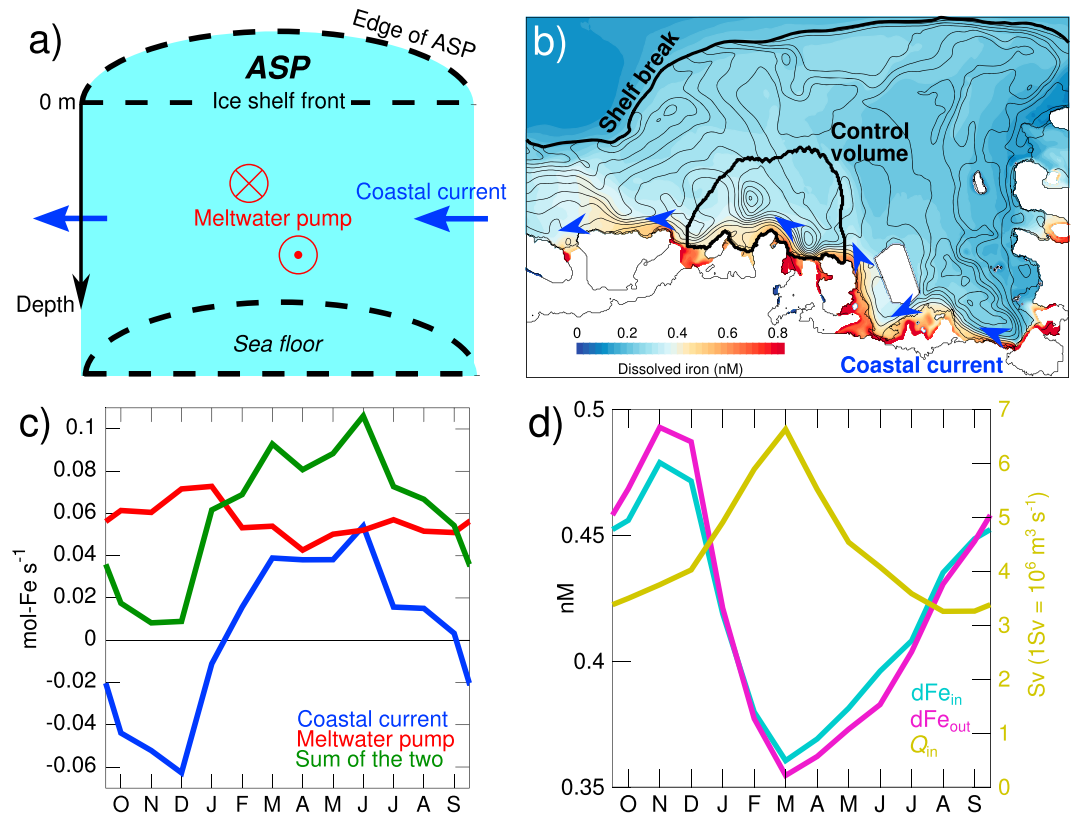
Figure 10. Fluxes of dissolved iron (dFe) across the control volume (illustrated in panel b and including the surface to the bottom). (a) Sketch illustrating the different fluxes across the faces of the volume. (b) Dissolved iron concentrations averaged over the upper 300 m (shading) and barotropic circulation on the shelf (streamlines; contour interval 0.2 Sv). Both are annual averages over 2006–2013. The coastal current is highlighted with blue arrows. (c) Net flux across the edge of the polynya (i.e., "coastal current," blue) or across the ice shelf front ("meltwater pump," red). Positive values indicate a net gain. (d) Contributions from lateral gradients (dFe_{in} − dFe_{out}) and volume transport (Q_{in}) to the variability of the coastal current's dFe flux. All values are averaged over 2006–2013. ASP = Amundsen Sea Polynya.

The contribution of the meltwater pump (which itself has contributions from both the melting glacial ice itself and deep sediment-sourced dFe from outside the ice shelf cavities) is fairly uniform over the year and dominates the supply of the polyna (Figure 10c), especially during the period of most active bloom growth. In contrast, the contribution of the coastal current varies widely over seasons. It removes dFe from the control volume in September–December and supplies dFe to the volume in February–August. The supply from the coastal current in March–June is comparable to that of the meltwater pump (~ 0.04 mol Fe/s; Figure 10c). Overall, the sum of these two inputs is comparable to the biological iron uptake during December–January but substantially smaller than the loss/gain associated with scavenging and remineralization (Figure 8a). Note that this "remineralization process" is how the model returns pFe to the dissolved state and iron desorption is not modeled explicitly (see section 2.2.4).

The complex seasonality of the coastal current is further examined by decomposing its flux of dFe (mol Fe/s) into two terms (equation (3)):

$$\text{Flux}_{\text{coastal current}}(t) = dFe_{in}(t)\,Q_{in}(t) - dFe_{out}(t)\,Q_{out}(t), \tag{3}$$

$$\approx Q_{in}(t)\left[dFe_{in}(t) - dFe_{out}(t)\right], \tag{4}$$

where $\text{Flux}_{\text{coastal current}}$ represents the blue curve of Figure 10c and Q_{in} (Q_{out}) is the volume of water entering (exiting) the edge of the control volume at time t. The terms dFe_{in}, dFe_{out} are the flux-weighted average dFe concentration associated with the inflow and outflow, respectively. The difference between these two dFe values represents the lateral gradient between the control volume and its surroundings. Since the shape of the control volume is constant except for negligible oscillations of the surface (i.e., $Q_{in} \approx Q_{out}$), we can
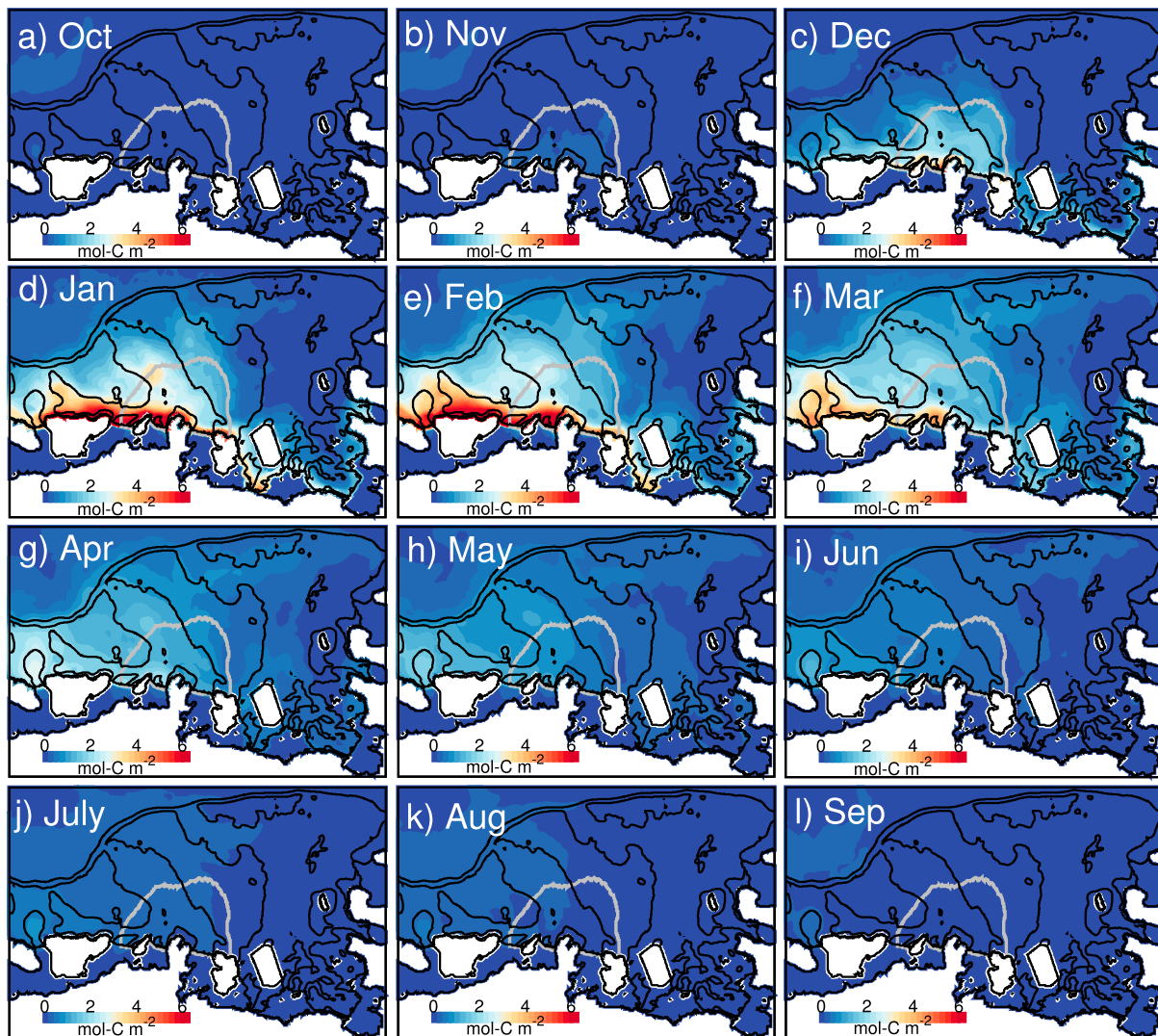
Figure 11. Vertically integrated particulate organic carbon concentrations (surface to bottom). The monthly fields (October to December, (a)-(l)) are averaged over years 2006–2013. Black contour lines represent the grounding line, ice shelf front, and 500- and 1,000-m isobaths. The gray contour line is the climatological extent of the polynya in January.

simplify equation (3) into a contribution (more precisely, a modulation) from volume transport (Q_{in}) and a contribution from the lateral gradient of dFe (dFe$_{in}$ − dFe$_{out}$; see equation (4)).

During the months of October–December, the control volume is characterized by dFe concentrations that are higher than in the surrounding areas (in large part due to inputs from glaciers; e.g., Figure 6) leading to dFe$_{in}$ < dFe$_{out}$ (Figure 10d). Then, as the summer bloom develops and removes dFe from the polynya, the lateral gradient reverses (dFe$_{in}$ > dFe$_{out}$). From May to June, dFe$_{in}$ remains higher than dFe$_{out}$ before the sign of the gradient reverses again in September. This seasonality of the lateral gradient is responsible for the seasonality of the coastal current dFe flux (Figure 10c). The contribution of the volume flux (Q_{in}) is secondary as it does not affect the sign of the dFe flux. The circulation (Figure 10b) remains qualitatively similar over the seasons, and Q_{in} appears to mostly follow the seasonal ice cover: Q_{in} speeds up in December–March as the ocean becomes exposed to winds and slows down in March–June as the ice thickens.

3.4. Vertical Flux of Particulate Organic Matter

The budget of bpFe (see section 3.2) revealed a horizontal transport of biogenic iron material out of the polynya between January and June. We now examine this horizontal transport for the nitrogen component and investigate how horizontal advection affects the fate of the particulate organic matter produced during the bloom. The simulated concentrations of PON are converted to POC (assuming a Redfield ratio) and
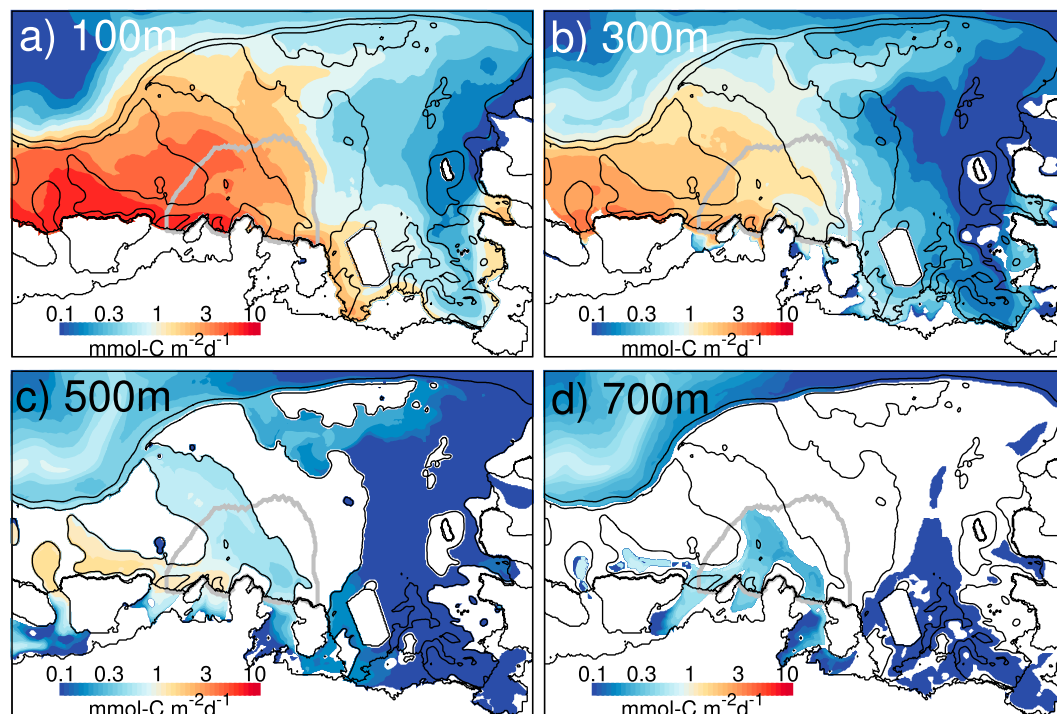
Figure 12. Average vertical carbon flux at four depth horizons (100m, 300m, 500m and 700m; (a)-(d)). The fluxes are are annually averaged over 2006–2013. Black contour lines represent the grounding line, ice shelf front, and 500- and 1,000-m isobaths. The gray contour line is the climatological extent of the polynya in January. Note the log scale used in the figure.

vertically integrated to produce monthly horizontal distributions (Figure 11). The POC concentrations increase rapidly in December with a horizontal distribution that reflects initially the surface biomass and the sea ice concentration (cf. Figure 11c with Figure 6). However, over the following months the biomass distribution becomes concentrated along the southern coast and extends itself westward beyond the area of open sea ice (Figure 11). This westward progression of the biomass reflects the westward coastal current that effectively "drains" the ASP (Figure 10b; Figure 8 of St-Laurent et al., 2017) by transporting surface and subsurface POC away from the polynya.

The vertically integrated POC concentrations outside of the coastal current are considerably more diffuse and decrease slowly after the summer bloom. This decrease occurs through remineralization (timescale of 3.3 months; see section 2) and also through sinking loss to the sediments. The latter process is examined for four depth horizons in Figure 12. The distributions of vertical flux are generally biased toward the west irrespective of the depth. This again reflects the westward coastal current and the westward expansion of the polynya during summer (e.g., Figure 5 of St-Laurent et al., 2017). Overall, the simulated vertical flux is maximum along the southern coast and west of the polynya. The flux decreases rapidly in magnitude with depth (because of remineralization) but remains substantial (~ 0.3 mmol C·m^{-2}·day^{-1}) down to 700 m in the glacial troughs of the continental shelf (Figure 12d). As discussed in section 2.6, the bulk of the simulated vertical flux occurs in February–June and is dominated by the large size fraction of detritus and its higher sinking velocity.

The vertical flux of POC represents a small but nonnegligible fraction of the POC budget on the continental shelf (Figure 13). POC exhibits a strong seasonality with a rapid increase between November and January (due to biological production), a peak inventory in February, and a gradual decrease over the subsequent months. The primary cause of this decrease is remineralization within the water column, which accounts for the bulk of the changes in POC between March and October (Figure 13b). On an annual average, the ratio between the losses due to vertical flux at the water-sediment interface ("sedimentation") and remineralization within the water column is ~0.17. The residual of the budget shows an additional loss between April and May (Figure 13b) that is unaccounted by remineralization or sedimentation. This additional loss
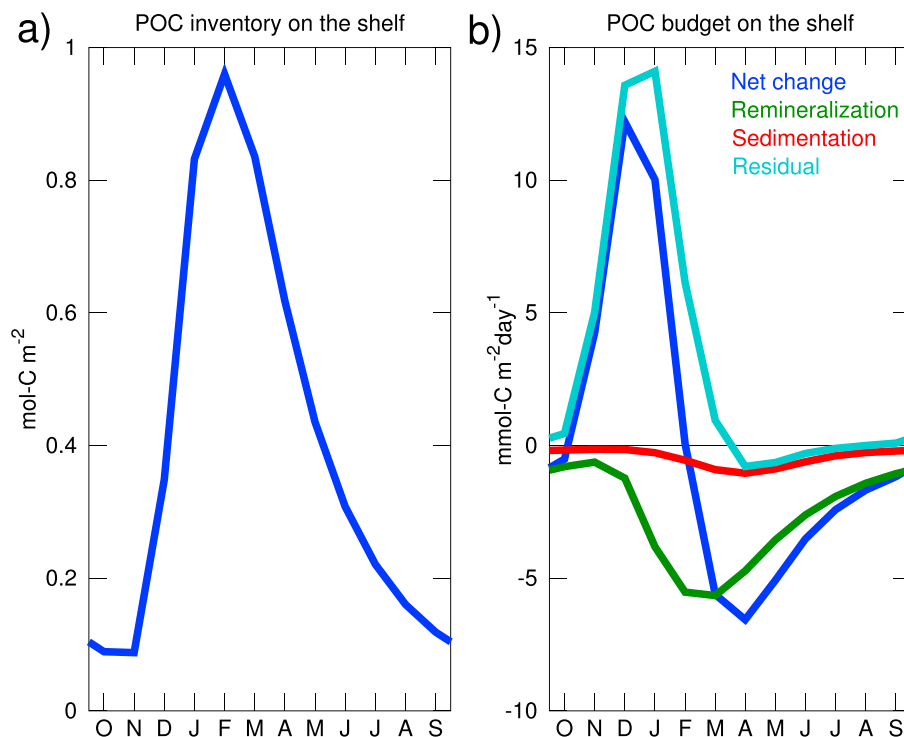
Figure 13. Seasonal budget for particulate organic carbon (POC) on the continental shelf of the model (see Figure 1 for its extent). (a) POC inventory integrated from the surface to the bottom and laterally averaged over the continental shelf. (b) Budget of POC for the same area. "Net change" is the temporal derivative of POC inventory. "Residual" is the change in POC that is not accounted by remineralization nor sedimentation. It includes primary production (mostly October to March) and the net lateral transport at the edges of the continental shelf. Values are averaged over 2006–2013.

represents a net lateral transport of POC out of the model's continental shelf (i.e., at the western edge of the model domain [Figure 1] or at the shelf break). This loss is smaller than sedimentation and its magnitude decreases rapidly after April in accord with the POC inventory (Figure 13b).

4. Discussion and Future Work

This study represents a first attempt at modeling the seasonal fluxes of iron and carbon in the ASP within the context of a high-resolution physical model forced by realistic atmospheric conditions, and including ocean interactions with both sea ice and ice shelves. The model represents explicitly the physical and bio-geochemical processes that link ice shelf melt, the summer phytoplankton bloom, and the vertical flux of organic carbon in the ASP.

It is informative to compare the results of this computationally intensive modeling study to the much faster 1-D approach that we used initially. While the 1-D model was able to simulate with good accuracy the vertical distribution of DIN at most of the stations occupied during the ASPIRE program, it was somewhat less successful simulating dFe distributions. One of several possible reasons for this was the assumption that the upper water column was uniform at the Winter Water dFe concentration of 0.3 nM, for all stations at the start of the growing season (1 October 2010). The 3-D model, in contrast, allows advection of dFe into the ASP from the westward flowing coastal current and from the inputs emanating from the cavities of the fringing ice shelves, driven by the meltwater pump. These inputs, combined with the eddy-dominated currents in the upper water column, lead to a spatially heterogeneous and generally higher dFe concentration (up to 0.8 nM in the southern ASP, Figure 6), providing higher initial dFe availability in the euphotic zone as the light increases early in the summer season. In addition, the coastal current and the meltwater pump continue to supply dFe to the upper water column over the course of the bloom development. The result of the higher initial dFe inventory and the continuous resupply of the meltwater pump is that dFe availability in the surface mixed layer of the control volume remains ≥0.3 (Figure 9a, equivalent to 0.13 nM) while the 1-D

reaches values as low as 0.1 equivalent to 0.03 nM). After the bloom, the dFe inventory of the 3-D model increases steadily from March through the winter with continued advective sources. While these model results need to be tested with additional observations, we believe the 3-D model reveals the magnitude of the advective dFe sources and their importance in making the ASP so unusually productive.

Still, some of the assumptions and simplifications made in the current 3-D model are worth emphasizing. Although comprehensive biogeochemical modules are readily available (e.g., Aumont et al., 2015; Jiang et al., 2013), they tend to involve a large number of parameters that are unconstrained in the case of the Amundsen Sea and may in fact be difficult to support with accurate values for any marine regime, given generally limited field observations. The paucity of data for the ASP motivates the relatively simple nitrate, plankton, zooplankton, and detritus model used here. While simple compared to the most complex biogeochemical models, our model captures some processes that are generally not parameterized in global-scale biogeochemical models that include iron. For example, we include two size classes of particles, aggregation/disaggregation exchange with larger, rarer, fast-sinking particles, and iron scavenging that is dependent on the concentration of the smaller particle class. Many global models, in contrast, have only one class of particles (Tagliabue et al., 2016) or a fixed rate for iron scavenging that is not dependent on the concentration of the host particles. Our parameterization of aggregation and disaggregation processes allows, for example, slow-sinking small particles to sink faster, effectively, so they can populate the deeper water column and effect iron scavenging there. In the intercomparison of Tagliabue et al. (2016), only one global model includes particle interactions at all, but in this case it involves colloids aggregating to a single particle class. Our model does not include colloids because we have, as yet, no observations of iron colloids in the ASP. Our model also does not include ligands, which means all forms of dFe are available for uptake and scavenging and also means that the model imposes no limit to dFe concentrations. Despite these simplifications, the modeled dFe concentrations neither become vanishing low (due to the lack of stabilizing ligand) nor unrealistically high (solubility not limited by ligand concentration). Our use of an invariant Fe:C ratio reflects the dominance of *Phaeocystis antarctica* in the ASP, and the assumption that it grows under iron stress for much of the duration of the bloom, but a lack of dependence on dFe availability or light puts our model in line with a minority of global iron biogeochemistry models (Tagliabue et al., 2016).

Despite these compromises, our model does very well in matching the measured dFe distributions (Figures 2–4). In the central ASP, dFe is higher, PON is higher, and DIN is drawn down much closer to observed levels, compared to the 1-D model results. We attribute this to the continuous iron inputs by the meltwater pump, combined with the seasonally variable coastal current flux (Figure 10c). These two sources act to build up the upper water column iron inventory in fall and winter, and continue to supply dFe to the ASP as the bloom is growing. As more data become available, future improvements should reexamine the role of ligands, the parameterization of scavenging, the two size classes of particulate matter, the possible role of iron colloids and the single phytoplankton pool with fixed iron demand. Finally, the model ignores the possible role of a large pool of nonbiogenic inorganic pFe (Planquette et al., 2013), which has the potential to interact with bioavailable iron pools. Nevertheless, the reasonable agreement with the ASPIRE data suggests that the current model captures the essential processes of the ASP.

This study focuses closely on the seasonal cycle of iron and carbon fluxes. The longer temporal trends and potentially important biogeochemical impacts of decreasing sea ice cover (Stammerjohn et al., 2015), changes in the configuration of the Thwaites Ice Tongue (MacGregor et al., 2012), and changes in the melting rate of ice shelves (Jenkins et al., 2018) thus remain to be examined. These scientific questions would require longer simulations (currently limited to 8 years; 2006–2013) and would require more realistic oceanic boundary conditions at the edges of the Amundsen Sea (the model currently uses a monthly climatology derived from Mazloff et al., 2010; see St-Laurent et al., 2017). Taking into account these longer-term drivers will be necessary to fully understand the causes of the interannual variability in the ASP production (Arrigo et al., 2012).

Air-sea CO_2 fluxes measured during the summer bloom (Mu et al., 2014) support the view that the ASP, and thus potentially other Antarctic polynyas, contributes significantly to the biological pump in this part of the world ocean. This contribution would depend, ultimately, on how much of the photosynthetically produced POC is sequestered in the deep ocean or sediments. Based on in situ measurements and instrument moorings, Lee et al. (2017) proposed that most of the carbon produced by the ASP would be flushed offshelf or converted into suspended/dissolved forms without being sequestered in sediments. The present simulations

suggest another possibility, namely, that the coastal circulation could decouple spatially the location of POC production from the location of its ultimate fate. Specifically, the westward coastal current transports the POC away from the highly productive central polynya, leading to relatively low carbon fluxes in the eastern ASP and larger carbon fluxes west of the ASP. More observations will be required to confirm this model prediction but it appears consistent with our knowledge of the coastal circulation (see the observations in Kim et al., 2016).

A final point is that the physical model may be hampered by the availability of geophysical data for the region. For example, serious discrepancies exist between the latest topographic data sets (Schaffer et al., 2016) and the multibeam data collected by icebreakers (see Kalén et al., 2016). This issue can profoundly affect the circulation and remains a major limitation for all ocean models of the Amundsen Sea.

5. Conclusions

The seasonal bloom of the ASP and its decline are controlled by the availability of both light and dFe in the model simulations. The seasonal budget of iron is dominated by exchanges between the dFe and bpFe pools driven largely by scavenging and remineralization; phytoplankton uptake has a smaller impact on the inventories of dissolved and pFe in the ASP as a whole. However, on annual timescales the ocean circulation contributes a substantial input of iron to the ASP. This lateral input of iron is mostly occurring at the ice shelf front and confirms the key role played by the buoyancy-driven circulation of melting ice shelf cavities (the meltwater pump). The simulations further suggest that the coastal circulation both provides iron derived from ice shelf cavities to the east and transports POC away from the productive central polynya, driving the highest vertical fluxes of POC to the western part of the ASP.

References

Alderkamp, A. C., Mills, M. M., van Dijken, G. L., Laan, P., Thuroczy, C., Gerringa, L. J., & Arrigo, K. R. (2012). Iron from melting glaciers fuels phytoplankton blooms in the Amundsen Sea (Southern Ocean): Phytoplankton characteristics and productivity. *Deep-Sea Research II*, *71-76*, 32–48. https://doi.org/10.1016/j.dsr2.2012.03.005

Alderkamp, A. C., van Dijken, G. L., Lowry, K. E., Connelly, T. L., Lagerstrom, M., Sherrell, R. M., & Arrigo, K. R. (2015). Fe availability drives phytoplankton photosynthesis rates during spring bloom in the Amundsen Sea Polynya, Antarctica. *Elementa: Science of the Anthropocene*, *3*(43), 43. https://doi.org/ 10.12952/journal.elementa.000043

Arrigo, K. R., Lowry, K. E., & van Dijken, G. L. (2012). Annual changes in sea ice and phytoplankton in polynyas of the Amundsen Sea, Antarctica. *Deep Sea Research II*, *71-76*, 5–15. https://doi.org/10.1016/j.dsr2.2012.03.006

Arrigo, K. R., van Dijken, G. L., & Strong, A. L. (2015). Environmental controls of marine productivity hot spots around Antarctica. *Journal of Geophysical Research: Oceans*, *120*, 5545–5565. https://doi.org/10.1002/2015JC010888

Aumont, O., Ethé, C., Tagliabue, A., Bopp, L., & Gehlen, M. (2015). PISCES-v2: An ocean biogeochemical model for carbon and ecosystem studies. *Geoscientific Model Development*, *8*, 465–2513. https://doi.org/10.5194/gmd-8-2465-2015

Becquevort, S., Smith, W. O., & Deep-Sea Research II (2001). Aggregation, sedimentation and biodegradability of phytoplankton-derived material during spring in the Ross Sea, Antarctica, *48*, 4155–4178.

Bruland, K. W., Middag, R., & Lohan, M. C. (2014). Controls of trace metals in seawater, *Treatise on geochemistry* (pp. 19–51). Hoboken, N.J.: Elsevier. https://doi.org/10.1016/B978-0-08-095975-7.00602-1

Budgell, W. P. (2005). Numerical simulation of ice-ocean variability in the Barents Sea region: Towards dynamical downscaling. *Ocean Dynamics*, *55*, 370–387. https://doi.org/10.1007/s10236-005-0008-3

Cavalieri, D., Markus, T., & Comiso, J. C. (2014). *AMSR-E/Aqua daily L3 12.5 km brightness temperature, sea ice concentration and snow depth polar grids. Version 3 for 2006–2011*. Boulder, Colorado USA: NASA DAAC at the National Snow and Ice Data Center. https://doi.org/10.5067/AMSR-E/AE_SI12.003

Clegg, S. L., Bacon, M. P., & Whitfield, M. (1991). Application of a generalized scavenging model to Thorium isotope and particle data at equatorial and high-latitude sites in the Pacific Ocean. *Journal Geophysical Research*, *96*(C11), 20655–20670.

De'Ath, R., Wadham, J. L., Monteiro, F., Le Brocq, A. M., Tranter, M., Ridgwell, A., & Raiswell, R. (2014). Antarctic ice sheet fertilises the Southern Ocean. *Biogeosciences*, *11*, 2635–2644. https://doi.org/10.5194/bg-11-2635-2014

Dee, D. P., Uppala, S. M., Simmons, A. J., Berrisford, P., Poli, P., Kobayashi, S., & Vitart, F. (2011). The ERA-Interim reanalysis: Configuration and performance of the data assimilation system. *Quarterly Journal of the Royal Meteorological Society*, *137*, 553–597. https://doi.org/10.1002/qj.828

Dinniman, M. S., Klinck, J. M., & Smith, W. O. Jr (2011). A model study of Circumpolar Deep Water on the west Antarctic Peninsula and Ross Sea continental shelves. *Deep Sea Research II*, *58*, 1508–1523. https://doi.org/10.1016/j.dsr2.2010.11.013

Ducklow, H. W., Wilson, S. E., Post, A. F., Stammerjohn, S. E., Erickson, M., Lee, S., & Yager, P. L. (2015). Particle flux on the continental shelf in the Amundsen Sea Polynya and Western Antarctic Peninsula. *Elementa: Science of the Anthropocene*, *3*, 46. https://doi.org/10.12952/journal.elementa.000046

Fennel, K., Wilkin, J., Levin, J., Moisan, J., O'Reilly, J., & Haidvogel, D. (2006). Nitrogen cycling in the Middle Atlantic Bight: Results from a three-dimensional model and implications for the North Atlantic nitrogen budget. *Global Biogeochemical Cycles*, *20*, GB3007. https://doi.org/10.1029/2005GB002456

Fiechter, J., Moore, A. M., Edwards, C. A., Bruland, K. W., Lorenzo, E. D., Lewis, C. V., & Hedstrom, K. (2009). Modeling iron limitation of primary production in the coastal Gulf of Alaska. *Deep-Sea Research*, *56*, 2503–2519. https://doi.org/10.1016/j.dsr.2009.02.010

Garcia, N. S., Sedwick, P. N., & DiTullio, G. R. (2009). Influence of irradiance and iron on the growth of colonial Phaeocystis antarctica: Implications for seasonal bloom dynamics in the Ross Sea, Antarctica. *Aquatic Microbial Ecology*, *57*, 203–220. https://doi.org/10.3354/ame01334

Gardner, A. S., Moholdt, G., Scambos, T., Fahnstock, M., Ligtenberg, S., van den Broeke, M., & Nilsson, J. (2018). Increased West Antarctic and unchanged East Antarctic ice discharge over the last 7 years. *The Cryosphere*, *12*, 521–547. https://doi.org/10.5194/tc-12-521-2018

Gerringa, L. J., Alderkamp, A. C., Laan, P., Thuroczy, C., De Baar, H. J., Mills, M. M., & Arrigo, K. R. (2012). Iron from melting glaciers fuels the phytoplankton blooms in Amundsen Sea (Southern Ocean): Iron biogeochemistry. *Deep-Sea Research II*, *71-76*, 16–31. https://doi.org/10.1016/j.dsr2.2012.03.007

Hahm, D., Rhee, T. S., Kim, H. C., Park, J., Kim, Y. N., Shin, H. C., & Lee, S. H. (2014). Spatial and temporal variation of net community production and its regulating factors in the Amundsen Sea, Antarctica. *Journal Geophysical Research: Oceans*, *119*, 2815–2826. https://doi.org/10.1002/2013JC009762

Hawkings, J. R., Wadham, J. L., Tranter, M., Raiswell, R., Benning, L. G., Statham, P. J., & Telling, J. (2014). Ice sheets as a significant source of highly reactive nanoparticulate iron to the oceans. *Nature of Communication*, *5*, 3929. https://doi.org/10.1038/ncomms4929

Holland, D. M., & Jenkins, A. (1999). Modeling thermodynamic ice–ocean interactions at the base of an ice shelf. *Journal Physical Oceanography*, *29*, 1787–1800.

Jenkins, A., Shoosmith, D., Dutrieux, P., Jacobs, S., Kim, T. W., Lee, S. H., & Stammerjohn, S. (2018). West Antarctic Ice Sheet retreat in the Amundsen Sea driven by decadal oceanic variability. *Nature Geoscience*, *11*, 733–738. https://doi.org/10.1038/s41561-018-0207-4

Jiang, M., Barbeau, K. A., Selph, K. E., Measures, C. I., Buck, K. N., Azam, F., & Zhou, M. (2013). The role of organic ligands in iron cycling and primary productivity in the Antarctic Peninsula: A modeling study. *Deep-Sea Research II*, *90*, 112–133. https://doi.org/10.1016/j.dsr2.2013.01.029

Jourdain, N. C., Molines, J. M., LeSommer, J., Mathiot, P., Chanut, J., deLavergne, C., & Madec, G. (2019). Simulating or prescribing the influence of tides on the Amundsen Sea ice shelves. *Ocean Modelling*, *133*, 44–45. https://doi.org/10.1016/j.ocemod.2018.11.001

Kalén, O., Assmann, K. M., Wåhlin, A. K., Ha, H. K., Kim, T. W., & Lee, S. H. (2016). Is the oceanic heat flux on the central Amundsen sea shelf caused by barotropic or baroclinic currents? *Deep-Sea Research II*, *123*, 7–15. https://doi.org/10.1016/j.dsr2.2015.07.014

Kim, B. K., Joo, H., Song, H. J., Yang, E. J., Lee, S. H., Hahm, D., & Lee, S. H. (2015). Large seasonal variation in phytoplankton production in the Amundsen Sea. *Polar Biology*, *38*, 319–331. https://doi.org/10.1007/s00300-014-1588-5

Kim, C., Kim, T., Cho, K., Ha, H. K., Lee, S., Kim, H., & Lee, J. (2016). Variability of the Antarctic coastal current in the Amundsen Sea. *Estuarine, Coastal and Shelf Science*, *181*, 123–133. https://doi.org/10.1016/j.ecss.2016.08.004

Lannuzel, D., Vancoppenolle, M., van der Merwe, P., de Jong, J., Meiners, K. M., Grotti, M., & Schoemann, V. (2016). Iron in sea ice: Review and new insights. *Elementa: Science of the Anthropocene*, *4*, 130. https://doi.org/ 10.12952/journal.elementa.000130

Lee, S., Hwang, J., Ducklow, H. W., Hahm, D., Lee, S. H., Kim, D., & Shin, H. C. (2017). Evidence of minimal carbon sequestration in the productive Amundsen Sea Polynya. *Geophysical Research Letter*, *44*, 7892–7899. https://doi.org/10.1002/2017GL074646

Lee, S. H., Kim, B. K., Yun, M. S., Joo, H., Yang, E. J., Kim, Y. N., & Lee, S. (2012). Spatial distribution of phytoplankton productivity in the Amundsen Sea, Antarctica. *Polar Biology*, *35*(11), 1721–1733. https://doi.org/10.1007/s00300-012-1220-5

MacGregor, J. A., Catania, G. A., Markowski, M. S., & Andrews, A. G. (2012). Widespread rifting and retreat of ice-shelf margins in the eastern Amundsen Sea Embayment between 1972 and 2011. *Journal of Glaciology*, *58*, 209. https://doi.org/10.3189/2012JoG11J262

Mazloff, M. R., Heimbach, P., & Wunsch, C. (2010). An eddy-permitting Southern Ocean state estimate. *Journal Physical Oceanography*, *40*(5), 880–899. https://doi.org/10.1175/2009jpo4236.1

Mellor, G. L., & Kantha, L. (1989). An ice-ocean coupled model. *Journal Geophysical Research*, *94*, 10,937–10,954.

Morales Maqueda, M. A., Willmott, A. J., & Biggs, N. R. T. (2004). Polynya dynamics: A review of observations and modeling. *Review Geophysics*, *42*, RG1004. https://doi.org/10.1029/2002RG000116

Mu, L., Stammerjohn, S. E., Lowry, K. E., & Yager, P. L. (2014). Spatial variability of surface pCO_2 and air-sea CO_2 flux in the Amundsen Sea Polynya, Antarctica. *Elementa: Sciice Anthropocene*, *2*, 36. https://doi.org/10.12952/journal.elementa.000036

Nihashi, S., & Ohshima, K. I. (2015). Circumpolar mapping of Antarctic Coastal Polynyas and Landfast Sea Ice: Relationship and variability. *Journal Climate*, *28*, 3650–2670. https://doi.org/10.1175/jcli-d-14-00369.1

Park, J., Kuzminov, F. I., Bailleul, B., Yang, E. J., Lee, S., Falkowski, P. G., & Gorbunov, M. Y. (2017). Light availability rather than Fe controls the magnitude of massive phytoplankton bloom in the Amundsen Sea Polynyas, Antarctica. *Limnology and Oceanography*, *62*(5), 2260–2276. https://doi.org/10.1002/lno.10565

Planquette, H., Sherrell, R. M., Stammerjohn, S., & Field, M. P. (2013). Particulate iron delivery to the water column of the Amundsen Sea, Antarctica. *Marine Chemistry*, *153*, 15–30. https://doi.org/10.1016/j.marchem.2013.04.006

Rignot, E., Jacobs, S., Mouginot, J., & Scheuchl, B. (2013). Ice-shelf melting around Antarctica. *Science*, *341*, 266–270. https://doi.org/10.1126/science.1235798

Schaffer, J., Timmermann, R., Arndt, J., Kristensen, S. S., Mayer, C., Morlighem, M., & Steinhage, D. (2016). A global, high-resolution data set of ice sheet topography, cavity geometry and ocean bathymetry. *Earth System Science Data Discussed*, *8*, 543–557. https://doi.org/10.5194/essd-8-543-2016

Shchepetkin, A. F., & McWilliams, J. C. (2005). The Regional Oceanic Modeling System (ROMS): A split-explicit, free-surface, topography-following-coordinate oceanic model. *Ocean Modeling*, *9*, 347–404. https://doi.org/10.1016/j.ocemod.2004.08.002

Sherrell, R. M., Annett, A. L., Fitzsimmons, J. N., Roccanova, V. J., & Meredith, M. P. (2018). A "shallow bathtub ring" of local sedimentary iron input maintains the Palmer Deep biological hotspot on the West Antarctic Peninsula shelf. *Philosophical Transactions of the Royal Society A*, *376*, 2122. https://doi.org/10.1098/rsta.2017.0171

Sherrell, R. M., Lagerstrom, M. E., Forsch, K. O., Stammerjohn, S. E., & Yager, P. L. (2015). Dynamics of dissolved iron and other bioactive trace metals (Mn, Ni, Cu, Zn) in the Amundsen Sea Polynya, Antarctica. *Elementa: Science of the Anthropocene*, *3*, 71. https://doi.org/10.12952/journal.elementa.000071

St-Laurent, P., Yager, P. L., Sherrell, R. M., Stammerjohn, S. E., & Dinniman, M. S. (2017). Pathways and supply of dissolved iron in the Amundsen Sea (Antarctica). *Journal of Geophysical Research: Oceans*, *122*, 7135–7162. https://doi.org/10.1002/2017jc013162

Stammerjohn, S. E., Maksym, T., Massom, R. A., Lowry, K. E., Arrigo, K. R., Yuan, X., & Yager, P. L. (2015). Seasonal sea ice changes in the Amundsen Sea, Antarctica, over the period of 1979–2014. *Elementa Science Anthropocene*, *3*, 55. https://doi.org/10.12952/journal.elementa.000055

Strzepek, R. F., Maldonado, M. T., Hunter, K. A., Frew, R. D., & Boyd, P. W. (2011). Adaptive strategies by Southern Ocean phytoplankton to lessen iron limitation: Uptake of organically complexed iron and reduced cellular iron requirements. *Limnology and Oceanography*, *56*(6), 1983–2002. https://doi.org/10.4319/lo.2011.56.6.1983

Tagliabue, A., Aumont, O., Death, R., Dunne, J. P., Dutkiewicz, S., Galbraith, E., & Yool, A. (2016). How well do global ocean biogeochemistry models simulate dissolved iron distributions? *Global Biogeochemical cycles*, *30*, 149–174. https://doi.org/10.1002/2015GB005289

Wadley, M. R., Jickells, T. D., & Heywood, K. J. (2014). The role of iron sources and transport for Southern Ocean productivity. *Deep-Sea Research I*, *87*, 82–94. https://doi.org/10.1016/j.dsr.2014.02.003

Wang, S., & Moore, J. K. (2011). Incorporating Phaeocystis into a Southern Ocean ecosystem model. *Journal Geophysical Research*, *116*, C01019. https://doi.org/10.1029/2009JC005817

Yager, P. L., Sherrell, R. M., Stammerjohn, S. E., Alderkamp, A. C., Schofield, O., Abrahamsen, E. P., & Wilson, S. (2012). ASPIRE: The Amundsen Sea Polynya International Research Expedition. *Oceanography*, *25*(3), 40–53. https://doi.org/10.5670/oceanog.2012.73

Yager, P. L., Sherrell, R. M., Stammerjohn, S. E., Ducklow, H. W., Schofield, O. M., Ingall, E. D., & van Dijken, G. L. (2016). A carbon budget for the Amundsen Sea Polynya, Antarctica: Estimating net community production and export in a highly productive polar ecosystem. *Elementa: Scienc Anthropocene*, *4*, 140. https://doi.org/10.12952/journal.elementa.000140

Yang, E. J., Jiang, Y., & Lee, S. (2016). Microzooplankton herbivory and community structure in the Amundsen Sea, Antarctica. *Deep-Sea Research II*, *123*, 58–68. https://doi.org/10.1016/j.dsr2.2015.06.001